

The Volcanic and Radial Expansion/Contraction History of the Moon Simulated by Numerical Models of Magmatism in the Convective Mantle

Ken'yo U^{1*}, Masanori Kameyama², and Masaki Ogawa¹

¹Department of Earth Sciences and Astronomy, The University of Tokyo, Komaba, Meguro, Japan
²Geodynamics Research Center, Ehime University, Matsuyama, Japan

Key Points:

- We numerically simulated magmatism in the convecting mantle of the Moon to understand its evolution
- Magma is generated in the deep mantle and ascends to the surface as partially molten fingers and plumes driven by melt-buoyancy
- Extension of partially molten regions by the fingers and plumes cause the observed expansion and active volcanism of the early Moon

arXiv:2303.16517v1 [astro-ph.EP] 29 Mar 2023

*“U” is the family name in the author Ken'yo U.

Corresponding author: Ken'yo U, u-kenyo0822@g.ecc.u-tokyo.ac.jp

Abstract

[To understand the evolution of the Moon, we numerically modeled mantle convection and magmatism in a two-dimensional polar rectangular mantle. Magmatism occurs as an upward permeable flow of magma generated by decompression melting through the convecting matrix. The mantle is assumed to be initially enriched in heat-producing elements (HPEs) and compositionally dense ilmenite-bearing cumulates (IBC) at its base. Here, we newly show that magma generation and migration play a crucial role in the calculated volcanic and radial expansion/contraction history. Magma is generated in the deep mantle by internal heating for the first several hundred million years. A large volume of the generated magma ascends to the surface as partially molten fingers and plumes driven by melt-buoyancy to cause a volcanic activity and radial expansion of the planet with the peak at 3.5-4 Gyr ago. Eventually, however, the planet begins to radially contract when the mantle solidifies by cooling from the surface boundary. As the mantle is cooled, the activity of partially molten plumes declines but continues for billions of years after the peak because some basal materials enriched in the dense IBC components hold HPEs. The calculated volcanic and radial expansion/contraction history is consistent with the observed history of the Moon. Our simulations suggest a substantial fraction of the mantle was solid, and there was a basal layer enriched in HPEs and the IBC components at the beginning of the history of the Moon.]

Plain Language Summary

[We developed a numerical model of magmatism in the convecting mantle to understand the volcanic and radial expansion/contraction history of the Moon. In the early period of the calculated history, magma is generated in the deep mantle and ascends to the surface as partially molten fingers and plumes driven by melt-buoyancy to cause volcanic activity. The extension of partially molten regions by magma ascent causes radial expansion of the planet. In its later period, however, the planet contracts with time because partially molten regions solidify as they are cooled from the surface boundary. The activity of partially molten plumes declines but continues for billions of years because some materials that host heat-producing elements are enriched in a compositionally dense component and remain in the deep mantle. The calculated history of radius change and volcanism is consistent with the observed lunar history. Our simulations suggest that a substantial fraction of the mantle was solid, and a dense layer enriched in heat-producing elements developed at the base of the mantle at the beginning of the history of the Moon.]

1 Introduction

Understanding the mantle evolution of the Moon that is behind its observed history of volcanic activity and radius change has been a long-standing issue in studies of the interiors of terrestrial planets (e.g., Solomon & Chaiken, 1976; Kirk & Stevenson, 1989; Shearer et al., 2006; Breuer & Moore, 2015). The Moon expanded globally by 0.5-5 km in its earlier history until around 3.8 Gyr ago as revealed by the gravity gradiometry data (Andrews-Hanna et al., 2013, 2014; Sawada et al., 2016; Liang & Andrews-Hanna, 2022), and it then globally contracted until today, as suggested from observations of tectonic features on the Moon (Yue et al., 2017; Frueh et al., 2023); some observations of fault scarps (thrust faults) suggest that the contraction for the past 100 Myr is around 1 km or less (e.g., Watters et al., 2010, 2015; Klimczak, 2015; Clark et al., 2017; van der Bogert et al., 2018; Matsuyama et al., 2021). The period when its radius reached the maximum coincides with that when the mare volcanism was active: mare volcanism became more active with time for the first several hundred million years of the lunar history, peaked at 3.5-3.8 Gyr ago, and then declined but continued until around 1.5 Gyr ago (e.g., Hiesinger et al., 2000, 2003; Morota et al., 2011; Whitten & Head, 2015). To clarify the mantle evolution that has caused the observed features of the lunar history, we developed a two-

dimensional (2-D) polar rectangular model of the lunar mantle evolution where mantle convection and magmatism that transport heat, mass, and incompatible heat-producing elements (HPEs) are considered.

Various numerical models of mantle evolution have been advanced to account for the observed radius change, in particular, the early expansion of the Moon (e.g., Solomon, 1986; Shearer et al., 2006). Classical spherically symmetric one-dimensional (1-D) models where the radius change occurs only thermally show that the early expansion is reproduced in the models when the temperature in the deep mantle is initially 1100 K or less; these models suggest that subsequent temperature rise of more than 700 K in the deep mantle due to internal heating caused the observed early expansion of the Moon (Solomon & Chaiken, 1976). In the model of Kirk and Stevenson (1989) that also takes volume change from compositional differentiation of the mantle into account, the early expansion occurs even when the initial temperature of the deep mantle is as high as 1200 K. Giant impact hypotheses for the origin of the Moon (e.g., Stevenson, 1987; Pritchard & Stevenson, 2000; Canup, 2004; Cuk & Stewart, 2012; Rufu et al., 2017; Lock et al., 2018), however, suggest a much higher initial temperature for the Moon. The mantle is expected to have been mostly molten to form the magma ocean immediately after the impact (e.g., Newsom & Taylor, 1989; Hosono et al., 2019). Even at the end of the mantle overturn, which is expected to have occurred after solidification of the magma ocean, the temperature of the deep mantle is still suggested to have been as high as about 1800–1900 K (e.g., Hess & Parmentier, 1995, 2001; Alley & Parmentier, 1998; Boukaré et al., 2018; H. Li et al., 2019). When such a high initial temperature is assumed, the early expansion of the Moon is difficult to reproduce in the classical thermal history models (e.g., Solomon & Chaiken, 1976; Solomon, 1986). The early expansion consistent with the observed history does not occur in three-dimensional (3-D) spherical models where mantle convection is also considered, too. In the models of N. Zhang et al. (2013a, 2013b), the early expansion does occur owing to internal heating, but the amplitude of the expansion is much smaller than the observed value (e.g., Andrews-Hanna et al., 2013), and the period when the expansion occurs is longer than 1 Gyr. In some models where the uppermost mantle is locally more enriched in HPEs on the nearside as observed for the Procellarum KREEP terrane, or PKT (Wieczorek & Phillips, 2000; Laneuville et al., 2013), the expansion occurs only on the nearside and is too large to account for the observed expansion (e.g., Liang & Andrews-Hanna, 2022). To understand the observed early expansion of the Moon, U et al. (2022) constructed a 1-D spherically symmetric model where volume change of the mantle by melting is considered in addition to thermal expansion. The mantle expands by a few kilometers for the first several hundred million years of the calculated history when partially molten regions extend in the mantle by internal heating, suggesting that melting of the mantle played an important role in the early expansion of the Moon. Yet, mantle convection is not considered in this model.

Various numerical models have been advanced to account for the long-lasting volcanism of the Moon, too (e.g., Shearer & Papike, 1999; Breuer & Moore, 2015). Some earlier models show that partially molten regions persist for billions of years in the upper mantle when the surface is covered with the crust enriched in HPEs or the blanketing regolith layer (Konrad & Spohn, 1997; Spohn et al., 2001; Ziethe et al., 2009). In models where the uppermost mantle in the nearside is more enriched in HPEs than that in the farside, the mantle has been partially molten for more than 3 billion years (Laneuville et al., 2013, 2014, 2018). In these models, however, the distribution of HPEs is spatially fixed or transported only by mantle convection, and extraction of HPEs from the mantle to the crust by magmatism, which is known to reduce the activity of magmatism (e.g., Cassen & Reynolds, 1973; Cassen et al., 1979; Ogawa, 2014), is not considered. In a model of Ogawa (2018a) where extraction of HPEs from the mantle by migrating magma is considered, partially molten regions in the mantle are all solidified, and magmatism stops within the first 2 Gyr of the calculated history, too early to account for the lunar mare volcanism (e.g., Hiesinger et al., 2003). It is also important to consider not only HPE-

extraction by migrating magma, but also the effects of structural evolution of the mantle in studies of the lunar volcanism (e.g., Hess & Parmentier, 1995; Zhong et al., 2000; Stegman et al., 2003; N. Zhang et al., 2013a; W. B. Zhang et al., 2022). In the early period of the Moon, a compositionally dense layer, which is enriched in HPEs and ilmenite-bearing cumulates (IBC) components, is suggested to have developed at the base of the mantle by crystal fractionation in the magma ocean and subsequent mantle overturn (e.g., Ringwood & Kesson, 1976; Elkins-Tanton et al., 2011; Moriarty III et al., 2021). Earlier mantle convection models suggest that the basal layer becomes thermally buoyant owing to internal heating and eventually migrates upward to the surface as hot plumes to cause mare volcanism after around 4 Gyr ago (e.g., Stegman et al., 2003). Whether or not the basal layer rises, however, depends on the compositional density contrast between the layer and the overlying mantle. These models assume conditions where the density contrast is low enough to allow the basal layer to rise by thermal convection (see Figure 1 in Le Bars and Davaille (2004)). The density contrast after mantle overturn is unclear and is influenced by the initial condition of overturn models (e.g., H. Li et al., 2019; Yu et al., 2019; W. B. Zhang et al., 2022); further studies with various density content are necessary to fully understand to effects of compositional mantle structure on volcanic history.

To understand the mantle evolution in the Moon that is constrained by its volcanic and radial expansion/contraction history, we extend the 1-D spherically symmetric model we developed earlier (U et al., 2022) to a 2-D polar rectangular model. In our previous model, we considered magma generation by internal heating and magma migration that transports heat, HPE, and mass as well as volume change of the mantle by melting. In addition to these effects, here in this study, we also include the effects of mantle convection. Heat and mass transport by mantle convection plays an important role in mantle evolution (e.g., Spohn et al., 2001; N. Zhang et al., 2017). Upwelling flows of mantle convection generate magma by decompression melting, which also affects mantle evolution of the planet (e.g., Ogawa, 2020). We also take the effects of compositional layering at the base of the mantle formed by the magma ocean and mantle overturn on the subsequent mantle evolution into account. This model is an extension of the one presented in Ogawa (2014, 2018a) in that we considered the volume change of mantle by melting, more systematically studied the effects of the initial condition, and calculated in a 2-D polar rectangle rather than rectangle.

2 Model description

A finite difference numerical code calculates the energy, mass, and momentum equations for mantle magmatism and mantle convection in a two-dimensional polar rectangular $R = [(r, \theta) \mid 385 \text{ km} \leq r \leq 1735 \text{ km}, 0 \leq \theta \leq \pi]$ under the Boussinesq approximation, where the inner and the outer radii correspond to the core and planetary radii, respectively, of the Moon (e.g., Weber et al., 2011; Yan et al., 2015; Viswanathan et al., 2019). The mantle contains incompatible heat-producing elements (HPEs) that decay with time. Mantle convection occurs as a convection of a Newtonian fluid whose viscosity strongly depends on temperature and is driven by thermal, compositional, and melt-buoyancy. The convecting materials are a binary eutectic system between olivine-rich materials and ilmenite-bearing cumulates (IBC). Magmatism occurs as generation of basaltic magma enriched in IBC materials and HPEs by decompression melting, internal heating, and upward permeable flow of the generated magma through the matrix (Vander Kaaden et al., 2015; McKenzie, 1984); the permeable flow is driven by the melt-buoyancy.

The crust of 35 km in thickness is placed on the top of the mantle (Wieczorek et al., 2013). The thermal diffusivity of the crust is about half that of the mantle, and hence the crust serves as a blanketing layer (Ziethe et al., 2009). The temperature is fixed at $T_{\text{sur}} = 270 \text{ K}$ on the surface boundary, while the core is modeled as a heat bath of uniform temperature; the vertical sidewalls are insulating. All of the boundaries are imper-

Table 1. The meanings of the symbols and their values.

Symbol	Meaning	Value
T_{sur}	Surface temperature	270 K
T_0	Solidus at the surface	1360 K
r_p	Radius of the surface	1735 km
r_c	Radius of the core-mantle boundary (CMB)	385 km
r_{crst}	Radius of the Moho	1695 km
ρ_0	Reference density	3300 kg m ⁻³
κ	Thermal diffusivity of the mantle	6×10^{-7} m ² s ⁻¹
κ_{edd}	Eddy diffusivity in largely molten region	100κ at $\phi > 0.4$
g_{sur}	Gravitational acceleration at the surface	1.62 m s ⁻²
g_c	Gravitational acceleration at the CMB	0.55 m s ⁻²
Δh	Latent heat of melting	657 kJ Kg ⁻¹
C_p	Specific heat	1240 J K ⁻¹ kg ⁻¹
η_0	Reference viscosity	$10^{20} - 10^{22}$ Pa s
η_{melt}	Melt viscosity	1 – 20 Pa s
E_T	Sensitivity of viscosity to temperature	11.3×10^{-3} K ⁻¹
ϕ_0	Reference melt-content	0.05
k_{ϕ_0}	Reference permeability	8.6×10^{-15} m ²
α_{m}	Thermal expansivity in the mantle	3×10^{-5} K ⁻¹
α_{c}	Thermal expansivity in the core	9×10^{-5} K ⁻¹

meable for both magma and matrix and are shear stress-free. In the initial condition, we assume that the deep mantle is more enriched in HPEs and IBC component than the shallower mantle as earlier models of mantle differentiation by the magma ocean and subsequent mantle overturn suggest (e.g., Ringwood & Kesson, 1976; Hess & Parmentier, 1995; Moriarty III et al., 2021). Several previous studies, however, suggest that a portion of the IBC materials enriched in HPEs persist just beneath the crust even after mantle overturn (e.g., Yu et al., 2019; Zhao et al., 2019; Schwinger & Breuer, 2022). Instead of explicitly simulating these remains of HPE-enriched materials, we assume that the crust is uniformly enriched in HPEs.

The numerical mesh employed for the calculation contains 128 (radial direction) times 256 (lateral direction) mesh points.

2.1 The properties of materials

The convecting material is a binary eutectic system. The composition is written as $A_\xi B_{1-\xi}$; the mantle materials are modeled as a mixture of olivine-rich materials A with a density of 3300 kg m⁻³ (Elkins-Tanton et al., 2011) and the IBC component B with a density of 3745 kg m⁻³ (Snyder et al., 1992; Shearer et al., 2006; Elkins-Tanton et al., 2011; Rapp & Draper, 2018). The eutectic composition is $A_{0.1}B_{0.9}$ which corresponds to the composition of the basaltic composition enriched in the IBC component (see Appendix for the detail of the thermodynamic formulation).

The density ρ is written as

$$\rho = (1 - \phi) \rho_s + \phi \rho_l. \quad (1)$$

where ρ_s is the density of solid-phase, ρ_l the density of melt-phase, and ϕ the melt-content. The densities depend on the temperature T and the content of the end-member A in the solid-phase ξ_s and that in the melt-phase ξ_l as

$$\rho_s = \rho_0 [1 - \alpha (T - T_{\text{sur}}) + \beta (1 - \xi_s)], \quad (2)$$

and

$$\rho_1 = \rho_0 \left\{ 1 - \alpha (T - T_{\text{sur}}) + \beta (1 - \xi_1) - \frac{\Delta v_1}{v_0} [1 + \beta (1 - \xi_1)] \right\}, \quad (3)$$

where ρ_0 is the reference density; α the thermal expansivity; $\beta = 0.135$ a constant estimated from the density of olivine-rich end-member A and that of the IBC end-member B. Temperature is calculated by the ‘reduced’ enthalpy h which is defined as

$$h = C_p T + \phi \Delta h (1 + G), \quad (4)$$

where C_p is the specific heat; Δh the latent heat of melting; G the function which depends on $\Delta v_1/v_0$ (see Eq. 10 below). $\Delta v_1/v_0$ expresses the amount of density reduction by melting as

$$\frac{\Delta v_1}{v_0} = \frac{1}{\rho_0} \left[\Delta \rho_\infty + \frac{\Delta \rho_{\text{zero}} - \Delta \rho_\infty}{(P/\lambda + 1)^2} \right]. \quad (5)$$

Here, $\Delta \rho_\infty/\rho_0 = 0.005$ is the dimensionless density difference between solid- and liquid-phases when pressure is infinity, and $\Delta \rho_{\text{zero}}/\rho_0 = 0.22$ that at zero-pressure. P is the pressure which defined as $P = -\int_{r_p}^r \rho_0 g dr$; the gravitational acceleration g depends on the depth as $g = g_{\text{sur}} - (g_{\text{sur}} - g_c) \frac{r_p - r}{r_p - r_c}$ (Garcia et al., 2011, 2012). We assumed the value of $\lambda = 16.42$ GPa so that the solidus temperature is calculated from the Clausius-Clapeyron relationship (see Eq. 9, 10 below) becomes close to that in the lunar mantle (Katz et al., 2003; Garcia et al., 2011, 2012).

Magma is generated by decompression melting and internal heating. The generated magma migrates upward as a permeable flow through the coexisting matrix driven by its buoyancy. Migrating magma transports heat, basaltic materials, and HPEs. The difference between the velocity of magma \mathbf{u} and that of matrix \mathbf{U} is proportional to the density difference between them as

$$\mathbf{u} - \mathbf{U} = \frac{k_\phi}{\phi \eta_{\text{melt}}} g (\rho_s - \rho_l) \mathbf{e}_r, \quad (6)$$

where k_ϕ is the permeability that depends on the melt-content ϕ as

$$k_\phi = k_{\phi_0} \left(\frac{\phi}{\phi_0} \right)^3 \quad (7)$$

(McKenzie, 1984) and \mathbf{e}_r is the unit vector in the radial direction. We assumed that $\phi_0 = 0.05$ and truncated ϕ at 0.4 for a numerical reason. The assumed range of k_{ϕ_0} given in Table 1 is based on the earlier works of McKenzie (1984) and Miller et al. (2014). In the top-most 150 km of the polar rectangular, we inserted $\phi' = \max(\phi, \phi_e)$ into the ϕ in Eq. 7 to mimic magma migration that occurs by crack propagation in the crust and the uppermost mantle of the Moon (Head & Wilson, 2017; Wilson & Head, 2017)

$$k_\phi = k_{\phi_0} \frac{[\max(\phi, \phi_e)]^3}{\phi_0^3}, \quad (8)$$

where $\phi_e = 0.035$ (Kameyama et al., 1996).

The solidus temperature T_{solidus} depends on the pressure as

$$T_{\text{solidus}} = T_0 (1 + G), \quad (9)$$

where

$$G = \frac{1}{\rho_0 \Delta h} \int_0^P \frac{\Delta v_1}{v_0} dP. \quad (10)$$

Here, T_0 is the solidus temperature at the surface (Katz et al., 2003).

The viscosity of the mantle η depends on temperature as

$$\eta = \eta_0 \exp [E_T (T_{\text{ref}} - T)], \quad (11)$$

where η_0 is the reference viscosity; $T_{\text{ref}} = 1575$ K is the reference temperature. E_T is the sensitivity of viscosity to temperature; we adopt the default value of E_T is $11.3 \times 10^{-3} \text{ K}^{-1}$ ($E_T^* = 6$, see Section 2.3 below) which implies that the viscosity decreases by a factor of 3 as temperature increases by 100 K. This range of viscosity is appropriate for Newtonian rheology to mimic thermal convection in mantle materials (Dumoulin et al., 1999). The value of E_T also prompts the ratio of viscosity at the surface boundary to that at the Moho discontinuity is a factor 5, which is a same value as that in some earlier studies obtained by Arrhenius temperature-dependence (e.g., N. Zhang et al., 2013a, 2017).

In the estimate of the lunar radial expansion, we consider the effect of melting as well as thermal expansion/contraction; the radius change ΔR is given by

$$\Delta R = \frac{1}{r_p} \left[\frac{\alpha_c \Delta T_c}{2} r_c^2 + \int_{r_c}^{r_p} \int_0^\pi \left(\alpha_m \Delta T + \frac{\Delta v_1}{v_0} \Delta \phi \right) r dr d\theta \right]. \quad (12)$$

In this equation, the first and second terms in the bracket of the right-hand side represent the volume changes of the core and the mantle, respectively. Here, α_c is the thermal expansivity of the core, $\Delta T_c \equiv T_c(t) - T_c(t=0)$ is the deviation of the temperature T_c in the core at the elapsed time t from its initial value $T_c(t=0)$, and $\Delta T_{\text{mid}} \equiv T(r, \theta, t) - T(r, \theta, t=0)$ and $\Delta \phi \equiv \phi(r, \theta, t) - \phi(r, \theta, t=0)$ are the deviations in the temperature T and melt-content ϕ in the mantle from their initial values, respectively. We assume that the initial condition in this model is the state of immediately after mantle overturn (see below), based on that the tectonic features of expansion/contraction in the crust are not recorded during the solidification of the magma ocean (Elkins-Tanton & Bercovici, 2014).

2.2 The initial condition

The initial thermo-chemical state of the mantle is specified by the initial distributions of heating rate q , bulk composition ξ_b , and temperature T . Here, the bulk composition is calculated from the composition of solid-phase ξ_s and that of ξ_l

$$\xi_b = (1 - \phi) \xi_s + \phi \xi_l. \quad (13)$$

Fig. 1 shows an example of the initial distributions of internal heating rate, composition, and temperature. This initial condition is motivated by earlier models of the mantle overturn that is expected to have occurred after the solidification of the magma ocean (e.g., Snyder et al., 1992; Alley & Parmentier, 1998; Boukaré et al., 2018; Rapp & Draper, 2018). In the last phase of crystal fractionation of the magma ocean, there remains a dense layer of the IBC with the concentration of urKREEP (K, rare earth elements, and P-rich material) at the top of the mantle. This layer is expected to sink down due to the gravitational instability at the base of the mantle (e.g., Ringwood & Kesson, 1976; Hess & Parmentier, 1995; de Vries et al., 2010).

The initial distribution of the temperature is obtained from that of the ‘reduced’ enthalpy (see Eq. 4). The initial distribution of the ‘reduced’ enthalpy is

$$h = \min (h_{\text{sur}}, h_{\text{mantle}}), \quad (14)$$

where

$$h_{\text{sur}} = C_p \left[T_{\text{sur}} + \delta_{\text{crst}} \left(1 - \frac{r}{r_p} \right) \right], \quad (15)$$

$$h_{\text{mantle}} = \begin{cases} C_p T_{\text{mid}} & \text{if } r > r_1 \\ C_p \left[T_{\text{mid}} + (T_c - T_{\text{mid}}) \left(\frac{r_1 - r}{r_1 - r_c} \right)^2 \right] & \text{if } r < r_1 \end{cases} . \quad (16)$$

Here, δ_{crst} and r_1 are the constants arbitrarily chosen to be $\delta_{\text{crst}} = 79.5 \times 10^3$ K to adopt the crust about 35 km thickness and $r_1 = 550$ km which is determined by assuming the post-overtun stratification, respectively (e.g., Boukaré et al., 2018; Mitchell, 2021). T_{mid} is the initial temperature in the mid-mantle; $T_c = 1875$ K the initial temperature of the core. The value of T_c is based on the assumption that the temperature of the core is hotter than the mantle at 4.4 Gyr ago (Alley & Parmentier, 1998; Boukaré et al., 2018; Morbidelli et al., 2018). We estimated the initial distribution of internal heat source $q = q_{\text{init}}$ in the mantle as $\int_{r_c}^{r_p} q_{\text{init}} r dr = \int_{r_c}^{r_p} q_0 r dr$, where $q_0 = 14.70$ pW kg $^{-1}$ is the average value of internal heating rate at the initial state of 4.4 Gyr ago estimated from Table 2 in U et al. (2022). We approximate the distribution of internal heating rate in the mantle described as

$$q_{\text{init}} = q_m + \Delta q \exp \left[-\frac{r - r_c}{l} \right], \quad (17)$$

where $q_m = 2.77$ pW kg $^{-1}$ is the internal heating rate of the olivine-rich materials in the mantle before mantle overturn (Yu et al., 2019); l the thickness of the basal layer which is enriched in the overturned materials; Δq is calculated from the assumption that the excess internal heating rate in the urKREEP Q_{ur} defined by:

$$Q_{\text{ur}} = \int_{r_c}^{r_{\text{crst}}} \Delta q \exp \left(\frac{r - r_c}{l} \right) r dr, \quad (18)$$

which value satisfies,

$$Q_{\text{ur}} = \int_{r_c}^{r_p} q_0 r dr - \left(\int_{r_{\text{crst}}}^{r_p} q_{\text{crst}} r dr + \int_{r_c}^{r_{\text{crst}}} \Delta q_m r dr \right). \quad (19)$$

Here, q_{crst} is the average initial heating rate of the crust which holds on the non-overtuned urKREEP (Yu et al., 2019; Zhao et al., 2019). We assume that the value of q_{crst} is obtained from the ratio of the concentration of the HPEs in the crust to that in the mantle written as

$$F_{\text{crst}}^* = \frac{\int_{r_{\text{crst}}}^{r_p} q_{\text{crst}} r dr}{\int_{r_c}^{r_p} q_0 r dr - \int_{r_{\text{crst}}}^{r_p} q_{\text{crst}} r dr}. \quad (20)$$

Furthermore, we calculated the initial distribution of the bulk composition ξ_b in the mantle using the assumption of that the overturned materials with the composition ($\xi_e = 0.1$) are 7.5 times more enriched in HPEs than the bulk Moon q_0 (Hess & Parmentier, 1995) as

$$\xi_b = 1 - \frac{\Delta q \exp[-(r - r_c)/l]}{7.5 q_0} (1 - \xi_e), \quad (21)$$

where in the crust, we assumed $\xi_b = 1$.

2.3 The parameter values

We carried out numerical experiments at various values of the non-dimensional reference permeability $M^* \equiv \frac{k_{\phi_0} \rho_0 g_{\text{sur}} L}{\kappa \eta_{\text{melt}}}$ (see Eq. A15) and the Rayleigh number $Ra \equiv \frac{\rho_0 \alpha_m (\Delta h / C_p) g_{\text{sur}} L^3}{\kappa \eta_0}$ (see Eq. A13), as well as the sensitivity of viscosity to temperature $E_T^* = E_T \Delta h / C_p$, the initial temperature in the mid-mantle T_{mid} , the thickness of the overturned layer $l^* = l/L$, and the ratio of the concentration of HPEs in the crust to that in the mantle F_{crst}^* , where $L = r_p - r_c$, is the depth of the mantle. The non-dimensional reference permeability M^* is proportional to $k_{\phi_0} / \eta_{\text{melt}}$ and expresses how easily the upward migration of magma takes place. We varied the values of M^* in the range of $5 \leq M^* \leq 100$, which

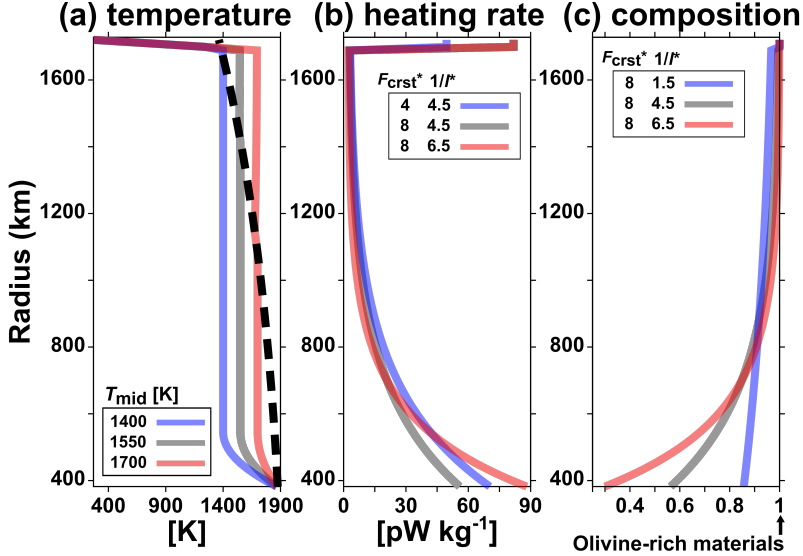


Figure 1. An illustration of the initial distributions of (a) temperature, (b) internal heating rate, and (c) bulk composition. In (a), the black dashed line is the solidus which is calculated by Eq. 9. The meaning of variable parameters T_{mid} , l^* , F_{crst}^* are described in Table 2.

Table 2. The variable parameters of the numerical models.

Variable parameter	Meaning	Range of value
M^*	Dimensionless reference permeability	5 to 100
Ra	Rayleigh number	2.15×10^4 to 10^6
E_T^*	Dimensionless sensitivity of viscosity to temperature	3 to 9
T_{mid}	Initial temperature in the mid-mantle	1400 to 1700 K
l^*	The thickness of the overturned layer after mantle overturn	1/6.5 to 1/1.5
F_{crst}^*	Concentration ratio of HPEs in the crust to the mantle	4 to 32

corresponds to the change in the viscosity η_{melt} of magma by a factor of 20 (1 to 20 Pa s). On the other hand, the Rayleigh number Ra is inversely proportional to the reference viscosity and expresses how readily mantle convection occurs. We assume that this value is in the range of 2.15×10^4 to 10^6 , which is estimated from a typical value of viscosity for mantle materials (Karato & Wu, 1993).

Other parameters listed in Table 2 are also varied to see how the numerical results depend on the thermal and compositional structure of the mantle assumed in the initial conditions. In the range of T_{mid} is decided by that of initial temperature in Laneuville et al. (2013) and that of post-overturn temperature in Boukaré et al. (2018). l^* is estimated from the density of the basal layer which is enriched in the overturned materials obtained by the results of previous overturn models (e.g., H. Li et al., 2019; Zhao et al., 2019). The thickness of the overturned layer is thinner and more concentrated in HPEs and the IBC component with a lower l^* . We also assume in the value of F_{crst}^* from that estimated in Konrad and Spohn (1997) and Spohn et al. (2001).

3 Results

3.1 The reference case

Figures 2-3 show the reference case of Case Ref calculated at the reference permeability $M^* = 100$; the Rayleigh number $Ra = 2.15 \times 10^6$, corresponding to $\eta_0 = 10^{20}$ Pa s; the sensitivity of viscosity on temperature $E_T^* = 6$; the initial temperature at depth $T_{\text{mid}} = 1550$ K; the initial thickness of the overturned layer $l^* = 4.5$; the initial crustal fraction of the HPEs $F_{\text{crst}}^* = 8$ (Table 2).

3.1.1 Thermal and structural evolution of the mantle

Figures 2 and 3 as well as the animation in supporting materials (Movie S1-4) illustrate how the mantle evolves dynamically by magmatism and mantle convection. The partially molten region in the uppermost mantle assumed in the initial condition shrinks with time owing to conductive cooling from the surface boundary (Figure 2b for 0.36 Gyr to 0.68 Gyr). In contrast, the temperature rises in the deep mantle that is enriched in HPEs in the initial condition, and magma is generated there within the first 150 Myr (Figures 2a and 3a; see also Movie S1-3). The distributions of melt-content, HPEs, and bulk composition in the deep mantle are laterally uniform at the beginning of the calculated evolutionary history of the mantle (Figure 2b-d for 0.36 Gyr). However, finger-like structures, or “melt-fingers”, eventually develop along the top of the partially molten region at a depth after around 0.4 Gyr. The fingertips are enriched in HPEs and the IBC component because of their transport by upward migrating magma (Figure 2 for 0.40 Gyr). Following the development of melt-fingers, partially molten plumes develop and ascend often along the fingers (see the arrows in Figure 2b) to induces peaks in the plot of rms-velocity in Figure 3d. Most of the partially molten plumes ascend to the uppermost mantle and reach the depth levels as shallow as around 25 km by 0.7 Gyr (Figure 2b and Table 3). These plumes in the uppermost mantle gradually solidify as they are cooled from the surface boundary. Some partially molten plumes, however, solidify in the mid and deep mantle (see the dashed circle in Figure 2c for 0.68 Gyr). The solidified materials enriched in HPEs and the IBC components then sink to the deep mantle because of their compositionally induced negative buoyancy (see Figure 2d; see also Movie S4 for around 0.60 Gyr and 0.84 Gyr). Internal heating by HPEs in these materials induces further partial melting in the deep mantle. As a consequence, partially molten plumes develop until around 4 Gyr, although they become fainter with time as the HPEs decline after around 2 Gyr (Figures 2b and 3b-d). Some materials in the uppermost mantle are enriched in HPEs and the IBC component by partially molten plumes (Figure 2c, d). These materials founder into the deep mantle owing to their compositionally induced negative buoyancy (see the arrow in Figure 2d). The return flow of this foundering generates magma that is not enriched in HPEs and by decompression melting (Figure 2b-d for 1.44 Gyr; see also Movie S2-4 for around 1.28 Gyr and 1.44 Gyr). We will discuss more about melt-fingers and partially molten plumes in Section 3.1.3, below.

3.1.2 radius change

Figure 4 shows how the planetary radius changes with time owing to the mantle evolution shown in Figures 2 and 3. The radius of a planet changes with time by two reasons, thermal expansion/contraction, and melting of the mantle (see Eq. 12), as indicated by the blue and red lines in the figure, respectively. The blue line in Figure 4 shows that the planet thermally expands by 0.4 km in the early history as the mantle is heated up and then contracts until the end of the calculation as the mantle is cooled (Figure 3b). On the other hand, the red line indicates the planet expands by 3 km for the first 0.7 Gyr owing to widespread partial melting of the mantle caused by melt-fingers and plumes (the peak [3] in Figure 4). After that, the planet gradually contracts with time as the mantle solidifies. Note that the contraction is not monotonous: slight expansion occurs

Table 3. The values of the parameters listed in Table2 and results.

Case #	M^*	Ra	E_T^*	T_{mid} [K]	$1/l^*$	F_{crst}^*	ΔR_{peak} [km]	$t_{\Delta R}$ [Gyr]	χ_{Gyr} [km Gyr $^{-1}$]	L_{ϕ} [km]
Ref	100	2.15×10^6	6	1550	4.5	8	3.00	0.66	-1.01	25
M50	50	2.15×10^6	6	1550	4.5	8	4.44	0.70	-1.33	185
M20	20	2.15×10^6	6	1550	4.5	8	6.62	0.89	-1.47	225
M5	5	2.15×10^6	6	1550	4.5	8	8.95	1.73	-1.78	200
Ra2.15e4	100	2.15×10^4	6	1550	4.5	8	3.84	1.04	-1.16	75
Ra2.15e5	100	2.15×10^5	6	1550	4.5	8	3.80	1.05	-1.17	60
Ra7.15e5	100	7.15×10^5	6	1550	4.5	8	3.53	0.83	-0.96	40
ET3	100	2.15×10^6	3	1550	4.5	8	3.06	0.78	-0.76	15
ET9	100	2.15×10^6	9	1550	4.5	8	3.30	0.66	-1.28	165
Tm1400	100	2.15×10^6	6	1400	4.5	8	3.62	1.36	-0.57	30
Tm1475	100	2.15×10^6	6	1475	4.5	8	3.34	1.13	-0.67	25
Tm1625	100	2.15×10^6	6	1625	4.5	8	3.80	0.50	-1.00	30
Tm1700	100	2.15×10^6	6	1700	4.5	8	4.23	0.42	-1.41	115
11.5	100	2.15×10^6	6	1550	1.5	8	3.01	1.04	-1.17	190
12.5	100	2.15×10^6	6	1550	2.5	8	3.66	0.86	-1.43	80
13.5	100	2.15×10^6	6	1550	3.5	8	3.51	0.69	-0.97	170
15.5	100	2.15×10^6	6	1550	5.5	8	2.92	0.85	-1.20	20
16.5	100	2.15×10^6	6	1550	6.5	8	2.50	0.62	-0.93	15
10	100	2.15×10^6	6	1550	0	8	0.22	1.45	-0.62	215
Fcrst4	100	2.15×10^6	6	1550	4.5	4	3.85	0.69	-1.23	25
Fcrst16	100	2.15×10^6	6	1550	4.5	16	1.69	1.07	-1.03	190
Fcrst32	100	2.15×10^6	6	1550	4.5	32	-0.50	1.46	-0.95	395
M50-Ra2.15e4	50	2.15×10^4	6	1550	4.5	8	5.25	0.79	-0.83	205
M20-Ra2.15e4	20	2.15×10^4	6	1550	4.5	8	8.91	1.35	-0.82	305
M5-Ra2.15e4	5	2.15×10^4	6	1550	4.5	8	12.21	3.36	-0.37	285
M0-Ra2.15e4	0	2.15×10^4	6	1550	4.5	8	15.32	4.40	1.21	375
M50-15.5	50	2.15×10^6	6	1550	5.5	8	4.00	0.73	-1.22	160
M20-15.5	20	2.15×10^6	6	1550	5.5	8	7.09	0.83	-1.12	210
M5-15.5	5	2.15×10^6	6	1550	5.5	8	9.00	1.80	-1.25	195
Tm1400-15.5	100	2.15×10^6	6	1400	5.5	8	3.86	1.12	-0.10	155
Tm1700-15.5	100	2.15×10^6	6	1700	5.5	8	4.09	0.35	-1.16	40
Tm1400-11.5	100	2.15×10^6	6	1400	1.5	8	4.91	1.68	-0.84	210
Tm1700-11.5	100	2.15×10^6	6	1700	1.5	8	-0.21	0.53	-1.08	105
Tm1400-15.5	5	2.15×10^6	6	1400	5.5	8	9.83	3.40	-0.13	270
Ra2.15e4-15.5	100	2.15×10^4	6	1550	5.5	8	3.44	1.09	-1.17	25
Ra2.15e5-15.5	100	2.15×10^5	6	1550	5.5	8	3.15	1.10	-1.17	25
M50-Ra4-15.5	50	2.15×10^4	6	1550	5.5	8	4.98	1.15	-1.17	175
M20-Ra4-15.5	20	2.15×10^4	6	1550	5.5	8	9.43	1.62	-0.91	310
M5-Ra4-15.5	5	2.15×10^4	6	1550	5.5	8	12.57	3.19	-0.37	290
M5-Ra5-15.5	5	2.15×10^5	6	1550	5.5	8	12.46	3.02	-0.19	285

Table 3. Continued.

Case #	M^*	Ra	E_T^*	T_{mid} [K]	$1/l^*$	F_{crst}^*	ΔR_{peak} [km]	$t_{\Delta R}$ [Gyr]	χ_{Gyr}	L_{ϕ} [km]
ET9-l5.5	100	2.15×10^6	9	1550	5.5	8	3.28	0.60	-0.87	85
l5.5-Fcrst16	100	2.15×10^6	6	1550	5.5	16	1.74	0.890	-0.85	185
l5.5-Fcrst32	100	2.15×10^6	6	1550	5.5	32	-0.21	1.30	-0.91	315
ET3-l5.5	100	2.15×10^6	3	1550	5.5	8	2.99	0.80	-1.03	20
ET3-l1.5	100	2.15×10^6	3	1550	1.5	8	4.00	1.11	-0.82	160
M5-ET3-l5.5	5	2.15×10^6	3	1550	5.5	8	10.40	2.34	-2.00	180
Ra4-ET3-l5.5	100	2.15×10^4	3	1550	5.5	8	3.88	1.12	-1.67	25
Ra4-ET9-l5.5	100	2.15×10^4	9	1550	5.5	8	3.00	0.66	-1.17	150
ET9-l1.5	100	2.15×10^6	9	1550	1.5	8	2.19	0.85	-1.39	160
M5-ET9-l5.5	5	2.15×10^6	9	1550	5.5	8	8.75	1.62	-1.91	185
Tm14-l5.5-Fcrst16	100	2.15×10^6	6	1400	5.5	16	2.46	1.06	0.07	225
Tm17-l5.5-Fcrst16	100	2.15×10^6	6	1700	5.5	16	2.93	0.45	-1.10	50
ET3-l5.5-Fcrst16	100	2.15×10^6	3	1550	5.5	16	1.96	0.83	-0.94	50
ET9-l5.5-Fcrst16	100	2.15×10^6	9	1550	5.5	16	1.80	0.80	-1.27	195
Ra4-l5.5-Fcrst16	100	2.15×10^4	6	1550	5.5	16	2.14	1.46	-1.10	100
Ra5-l5.5-Fcrst16	100	2.15×10^5	6	1550	5.5	16	2.06	1.58	-0.86	115
l1.5-Fcrst16	100	2.15×10^6	6	1550	1.5	16	0.83	1.45	-0.97	90
l3.5-Fcrst16	100	2.15×10^6	6	1550	3.5	16	1.88	0.98	-0.69	185
M5-l5.5-Fcrst16	5	2.15×10^6	6	1550	5.5	16	4.37	1.79	-0.71	240
M20-l5.5-Fcrst16	20	2.15×10^6	6	1550	5.5	16	3.63	1.07	-0.60	260
M50-l5.5-Fcrst16	50	2.15×10^6	6	1550	5.5	16	2.65	0.80	-1.05	205
No-conv-HPeS-Mass-tr	100	2.15×10^2	6	1550	4.5	8	-0.65	1.11	-0.71	195
No-HPeS-Mass-tr	100	2.15×10^6	6	1550	4.5	8	-4.12	0.49	-0.80	20
No-Mass-tr	100	2.15×10^6	6	1550	4.5	8	-5.01	0.55	-1.30	15
beta07-Ref ($\beta = 0.067$)	100	2.15×10^6	6	1550	4.5	8	-0.60	2.38	-0.85	20

ΔR_{peak} and $t_{\Delta R}$ stands for the magnitude and timing of the peak of radial expansion, respectively; χ_{Gyr} the con- traction rate for the past 1 Gyr obtained by least-squares method; L_{ϕ} the shallowest depth levels of partially molten regions other than that in the initial state.

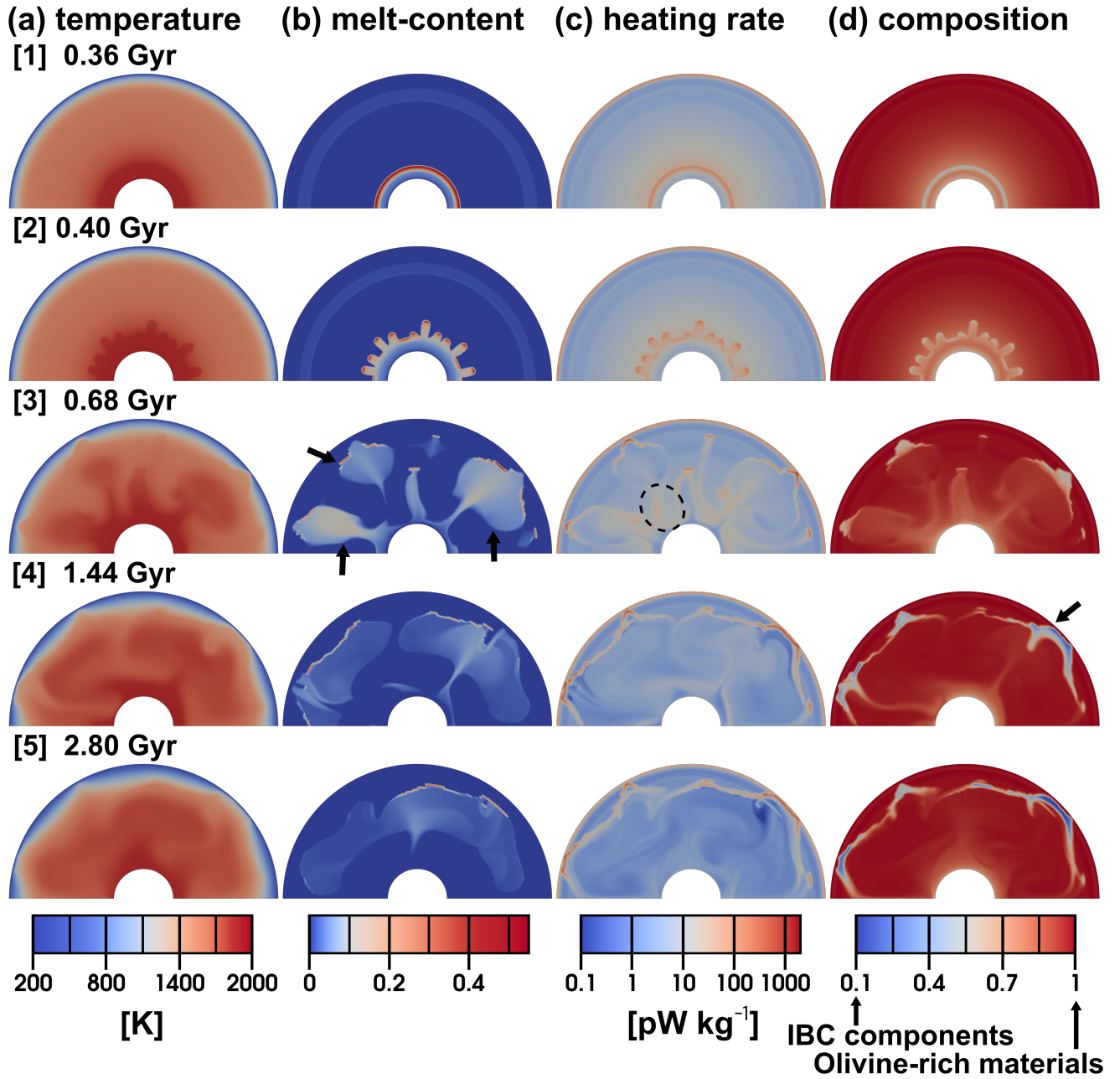


Figure 2. Snapshots of the distributions of (a) temperature T , (b) melt-content ϕ , (c) internal heating rate q , and (d) composition ξ_b calculated for Case Ref where $M^* = 100$; $Ra = 2.15 \times 10^6$, corresponding to $\eta_0 = 10^{20}$ Pa s; $E_T^* = 3$; $T_{\text{mid}} = 1550$ K; $l^* = 4.5$; $F_{\text{crst}}^* = 8$. The elapsed times are indicated in the figure. In (d), the blue color stands for the IBC component, while the red color for the olivine-rich end-member. The numbers [1] to [5] correspond with those of Figure 4.

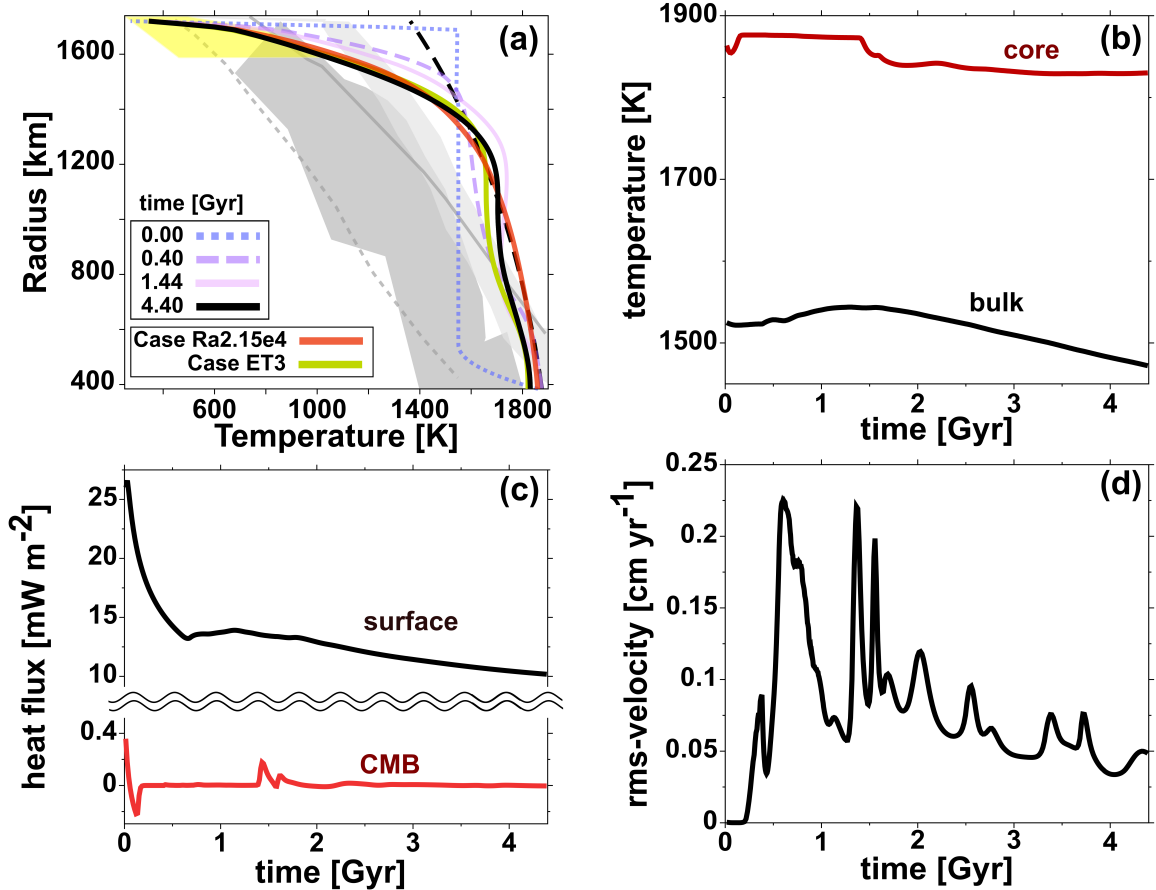


Figure 3. (a) The horizontal averages of the temperature-distributions at various elapsed times for Case Ref. Also shown are the horizontally averaged temperature at 4.4 Gyr for Case Ra2.15e4 ($Ra = 2.15 \times 10^4$) and ET3 ($E_T^* = 3$). In (a), the gray and light-gray areas are the temperature distributions in today's lunar mantle inferred by Khan et al. (2006) and Khan et al. (2014), respectively; the yellow areas are those estimated from the heat flux at the surface (Siegler & Smrekar, 2014; Siegler et al., 2022); the gray lines are those estimated under the assumption that the mantle consists of dry olivine (the solid line) and wet olivine with 0.01 wt % H_2O (the dashed line) by Karato (2013). Also shown are (b) the average temperature in the mantle (bulk) and the temperature of the core; (c) the horizontal average of heat flux on the surface and the core-mantle boundary (CMB); (d) the root-mean-square average of matrix-velocity in the mantle all plotted against time.

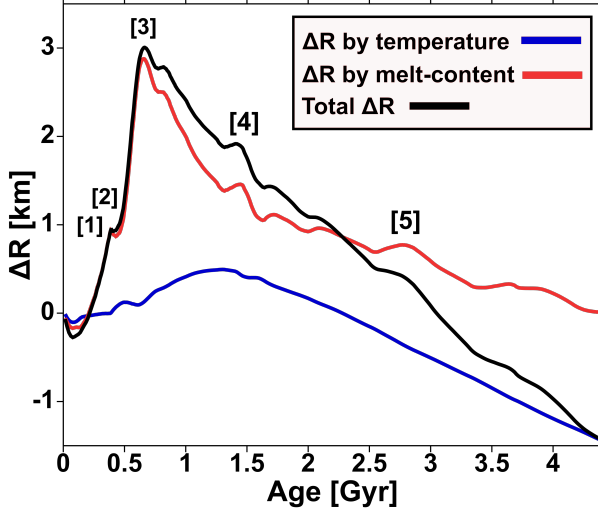


Figure 4. The history of radius change of planet calculated in the reference case (Case Ref). The radius change ΔR is defined by Eq. 12; the blue and red lines indicate the contribution of thermal expansion/contraction and melting, respectively, to the total radius change (the black line). The numbers [1] to [5] correspond with those of Figure 2.

several times when partially molten plumes develop (see [4] and [5] in Figures 2 and 4). As a whole, the black line in Figure 4 indicates that the planet radially expands by about 3 km during the first 0.7 Gyr and then contracts at the rate of around -1.0 km Gyr^{-1} until the end of the calculated history (Table 3).

3.1.3 Melt-fingers and partially molten plumes

To understand why melt-fingers grow from the partially molten region at depths at around 0.4 Gyr in Figure 2a, b, we delineate the velocity field of matrix around a nascent finger in Figure 5a (see the bump indicated by the yellow arrow). Figure 5 for 0.38 Gyr shows that melt-fingers develop and grow upward owing to matrix-expansion around the fingertip caused by injection of upward migrating magma. Indeed, the matrix velocity around the fingertips diverges as indicated by the arrows in Figure 5b. (We recalculated melt-fingers on a mesh with twice higher resolution and confirmed that fingers still grow; melt-fingers are not an artifact of numerical instability.)

After 100 Myr from the development of melt-fingers, partially molten plumes grow owing to the melt-buoyancy (see in Figure 5 for 0.48 Gyr). The stem of melt-finger indicated by the yellow dashed circle in Figure 5a becomes thicker with time as the melt that migrates upward from the partially molten layer at depth accumulates. Because of the buoyancy of accumulated melt, both the matrix and melt migrate upward (Figure 5): the thickened area ascends as a plume at 0.48 Gyr.

3.2 The occurrence of melt-fingers and partially molten plumes

To understand under what condition melt-fingers and partially molten plumes observed in the reference case grow, we calculated the model at various values of the reference permeability M^* , and the Rayleigh number Ra .

The reference permeability M^* influences the growth of melt-fingers; the snapshots of Case M5 ($M^* = 5$ and other parameters fixed at their default values) illustrate that

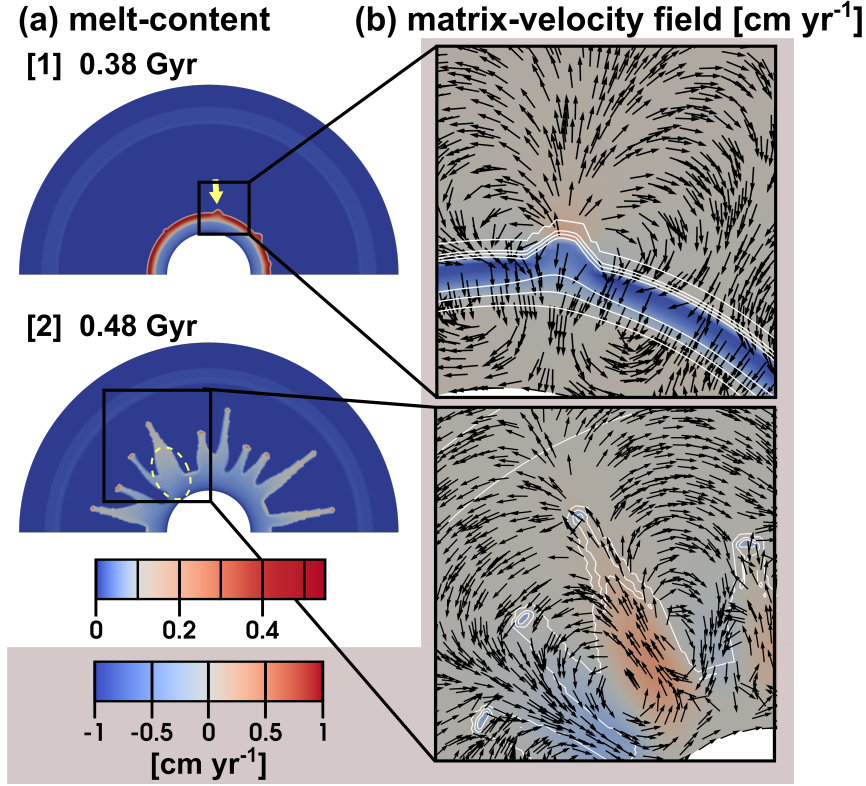


Figure 5. Snapshots of the (a) melt-content ϕ and (b) matrix-velocity field in the reference case (Case Ref). In (b), the red and blue colors show the regions where the convective flow points upward and downward, respectively; the arrows express the direction of convective flow but not its magnitude. The contour lines show the ϕ -distribution with the contour interval of 0.1 starting from 0.

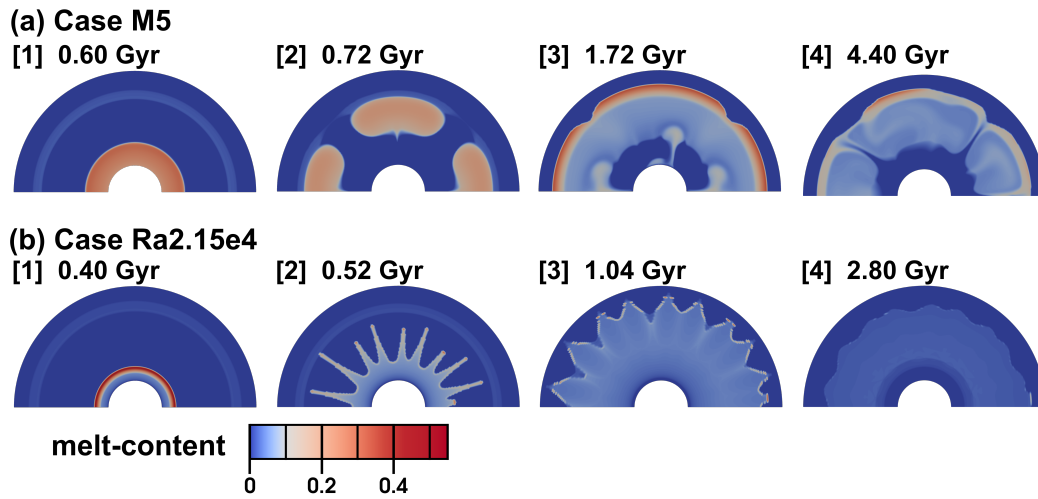


Figure 6. Snapshots of the distributions of melt-content ϕ calculated in cases with (a) a reduced reference permeability (Case M5) and (b) a reduced Rayleigh number (Case Ra2.15e4). The numbers [1] to [5] correspond with those of Figure 8a, e.

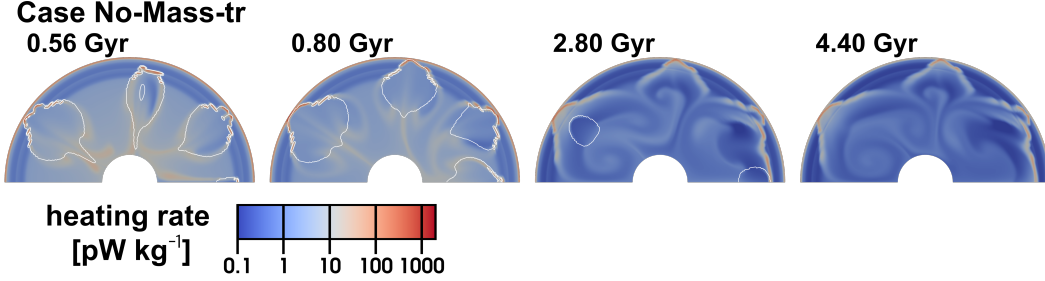


Figure 7. Snapshots of the distributions of internal heating rate q calculated in a case where the composition ξ_b is kept uniform (Case No-Mass-tr). The contour lines show the distribution of melt-content with contour level of 0 and 0.1.

the melt-fingers do not occur at the lower reference permeability of this case (Figure 6a). Instead, partially molten plumes that are broader than those observed in the reference case rise to the depth levels of 200 km by around 1.7 Gyr (Figure 6a for 1.72 Gyr and Table 3). The plumes laterally extend and form a continuous layer of partially molten materials (Figure 6a). The partially molten layer then solidifies upon cooling from the surface boundary; the layer, however, still remains in the mid-mantle at 4.4 Gyr (Figure 6a). We observed that melt-fingers grow only in the cases calculated at $M^* \geq 50$ (see Figure S1 in supporting materials).

At $M^* = 100$, we also calculated several models at various values of Ra in the range from 2.15×10^2 to 2.15×10^6 (Table 3); we found that melt-fingers develop regardless of the values of Ra , implying that buoyancy does not play any role in the growth of melt-fingers (Figures 6b and S2 in supporting materials). This result reinforces the above conclusion that melt-fingers develop because of matrix-expansion around the fingertip (Section 3.1.3). We further calculated a case (Case No-conv-HPes-Mass-tr) with the partition coefficient of HPes $D = 1$ in Eq. A11 (see Appendix) and a model that starts from a compositionally uniform mantle with the bulk composition $\xi_b = \xi_e$ (Table 3) and found that the development of melt-fingers does not depend on these parameters.

In contrast to melt-fingers, the growth of partially molten plumes depends on the Rayleigh number. At $Ra = 2.15 \times 10^4$ that is lower than Ra of the reference case by a factor of 100 (Case Ra2.15e4), only melt-fingers develop, and partially molten plumes do not grow (Figure 6b). Melt-fingers grow upward to the depth level of around 75 km by around 1.0 Gyr (Figure 6b and Table 3) and then expand laterally, to make the most part of the mantle partially molten (Figure 6b for 1.04 Gyr). After that, the partially molten region shrinks monotonously with time owing to conductive cooling from the surface boundary (Figure 6b for 2.80 Gyr). We found that partially molten plumes grow only in the cases calculated at $Ra \geq 7.15 \times 10^5$ (see Figure S2). This result reinforces that partially molten plumes are driven by their buoyancy.

3.3 The effect of the initial distribution of mantle composition

To see how plume magmatism continues for billions of years in the reference case (Figure 2), we further calculated Case No-Mass-tr where we assumed a compositionally uniform mantle with the bulk composition $\xi_b = \xi_e$ in the initial condition (Table 3). In this case, most of partially molten plumes ascend to the uppermost mantle by around 0.8 Gyr, and plume activity declines after that (Figure 7). The early decline of plume activity results from the early extraction of HPes from the deep mantle where magma is mostly generated. In contrast, HPE-extraction by early plume magmatism is not so

efficient in the reference case where the deep mantle is assumed to be enriched in the dense IBC-component in the initial condition (see Section 3.1.1). The duration time of plume activity depends on the initial distribution of the dense IBC-component.

3.4 Dependence of radial expansion on model parameters

We further carried out numerical experiments to show how the radial expansion-history depends on the model parameters: the reference permeability M^* ; the Rayleigh number Ra ; the sensitivity of viscosity to temperature E_T^* ; the initial mid-mantle temperature T_{mid} ; the thickness of the overturned layer l^* ; the initial concentration ratio of the HPEs in the crust to the mantle F_{crst}^* (Figure 8 and Table 3).

Among the parameters, the reference permeability M^* influences the expansion-history most strongly (Figure 8a); a lower M^* leads to a later peak of expansion with a larger amplitude. The larger expansion is due to a more slowly migrating magma that retains HPEs in the deep mantle for a longer period, and allows more heat to build up in the mantle (see Figure 6a and Table 3). The initial ratio of HPE-concentration in the crust to that in the mantle F_{crst}^* also substantially influences the magnitude of radial expansion (Figure 8b); a higher F_{crst}^* reduces radial expansion because the mantle is more depleted in HPEs and less magma is generated in the deep mantle. The initial mid-mantle temperature T_{mid} affects only the timing of radial expansion as shown in Figure 8c. A higher T_{mid} leads to an earlier peak of expansion because it implies an earlier generation of partially molten regions in the deep mantle and earlier extension of the regions into the uppermost mantle. The thickness of the overturned layer l^* has an effect on the beginning of radial expansion (Figure 8d). A higher $1/l^*$ where the deep mantle is more enriched in HPEs induces an earlier beginning of the expansion. Note that in Case 10 where HPEs and the composition ξ_b are uniform in the whole mantle ($1/l^* = 0$), the amplitude of that is smaller than in cases where the overturned layer is considered (Figure 8d). This is because enough magma generation does not occur to cause the early expansion in Case 10. Conversely, although the horizontal averages of the temperature-distributions depend on the values of Ra and E_T^* (Figure 3a), the dependences of expansion-history on the Rayleigh number Ra and the sensitivity of viscosity to temperature E_T^* are negligible as shown in Figure 8e and f.

4 Discussions

Figure 9 illustrates how the mantle evolves in the reference case shown in Figures 2-4. The partially molten region in the uppermost mantle shrinks with time, whereas that in the deep mantle expands on the earliest stage of the calculated history (Figure 9a). Melt-fingers then develop along the top of the partially molten region at depth, and the fingers extend upward (Figure 9b). After the growth of melt-fingers, partially molten plumes driven by melt-buoyancy rise to the uppermost mantle to cause plume magmatism (Figure 9c). The planet expands in the stage of Figure 9a-c because of melting of the mantle. These partially molten plumes transport HPEs and the IBC component from the deep mantle to the uppermost mantle. The plume magmatism then declines with time after around 2 Gyr of the calculated history because of depletion of HPEs in the deep mantle (Figure 9d). In the later period of the calculated history, the planet gradually contracts by cooling and solidification of the partially molten mantle. The reference case fits in with the observed history of the Moon the most among the models calculated here as we will discuss in Section 4.2.

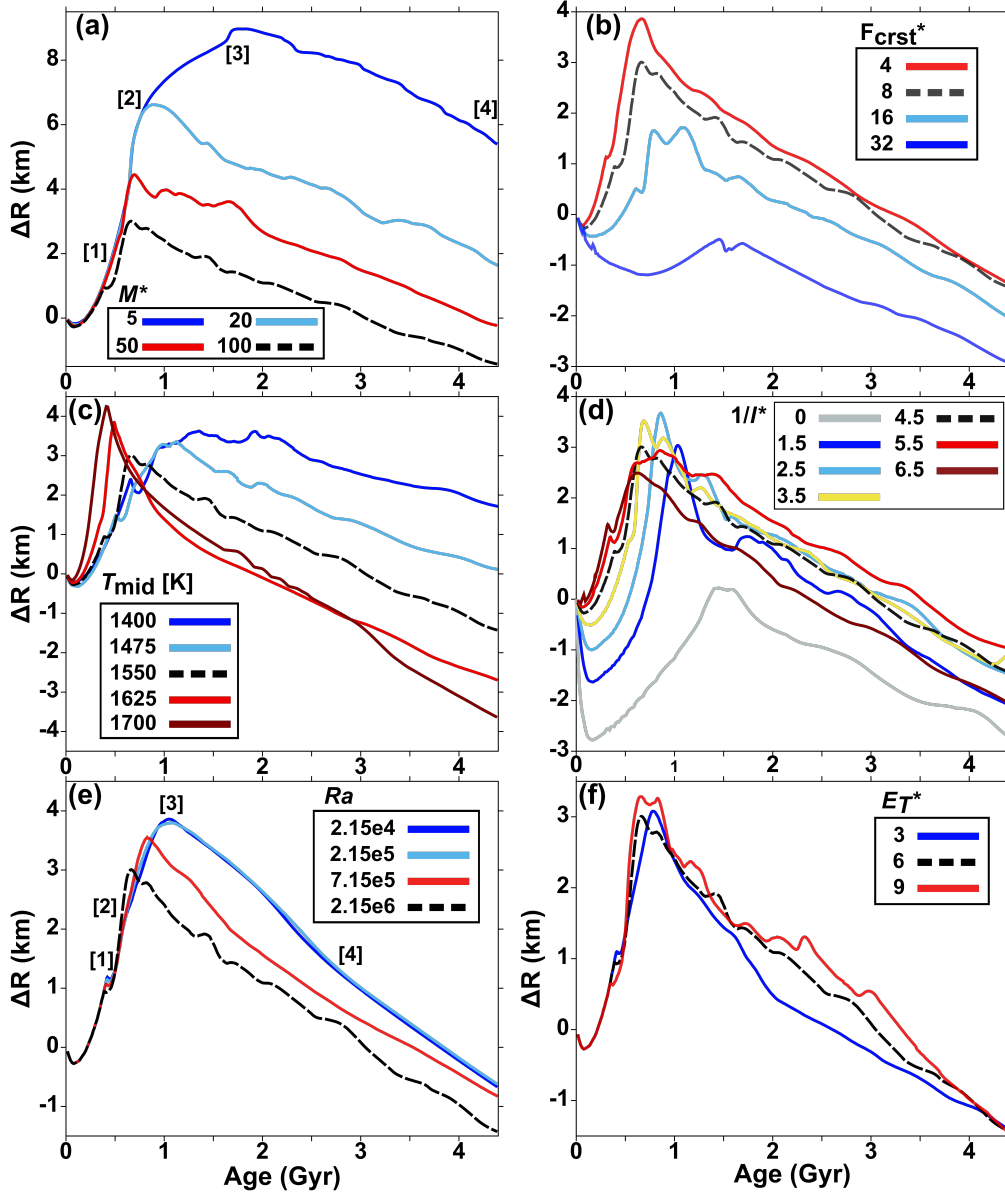


Figure 8. Plots of radius change against time calculated at various values of (a) the reference permeability M^* , (b) the initial crustal fraction of the HPEs F_{crst}^* , (c) the initial temperature in the mid mantle T_{mid} , (d) the thickness of the overturned layer l^* , (e) the Rayleigh number Ra , and (f) the sensitivity of viscosity to temperature E_T^* . The dotted lines show the reference case (Case Ref) presented in Figure 2-4. In (a) and (e), the numbers [1] to [5] correspond with those of Figure 6a and b, respectively.

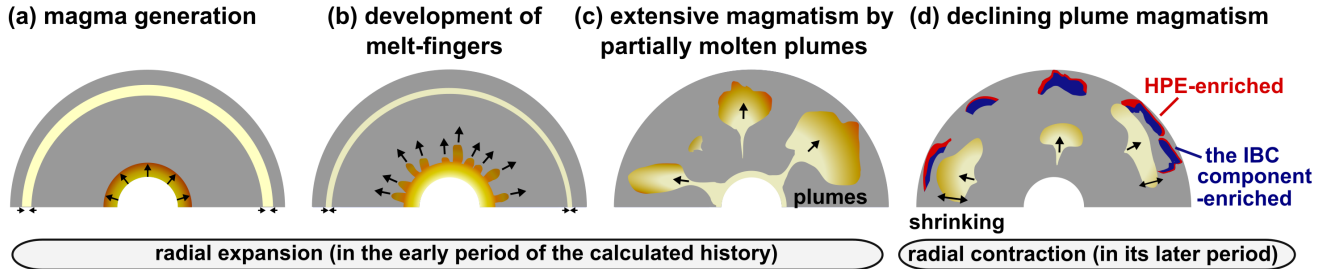


Figure 9. An illustration of the thermal and structural history of the lunar mantle inferred from our numerical study. The yellow color stands for melting.

4.1 Comparisons with earlier models

4.1.1 The mantle evolution caused by magmatism and convection

A comparison with earlier classical 1-D models of lunar thermal history in the literature shows the crucial role that heat transport by migrating magma and mantle convection plays in the reference case. In earlier 1-D models where only internal heating and thermal conduction are considered, the temperature in the deep mantle monotonously increases to the solidus temperature due to internal heating, while the lithosphere monotonously thickens with time owing to cooling from the surface boundary throughout the calculated history (e.g., Wood, 1972; Solomon & Toksöz, 1973; Toksöz & Solomon, 1973; Solomon & Chaiken, 1976). These models show that the deep mantle becomes extensively molten and the lithosphere becomes as thick as around 600 km at present. In our reference case where heat transport by migrating magma and mantle convection is also considered, however, the temperature is below the solidus in most part of the deep mantle, and the thickness of the lithosphere is by less than around 350 km at 4.4 Gyr (Figure 3a).

A comparison with earlier 2- or 3-D models of the lunar thermal history where mantle convection also is considered, on the other hand, shows the crucial roles that magma plays in heat transport in the convecting mantle. The vigor of thermally driven mantle convection is controlled by the distance from the threshold for the onset of thermal convection on the plane of the Rayleigh number Ra_d and the viscosity contrast η_{top}/η_{bot} shown in Figure 10 (Yanagisawa et al., 2016). As shown in the figure, our reference case (Case Ref) is calculated under the condition that thermally driven mantle convection is more sluggish than that of the earlier models of lunar mantle convection Z-E100, Z-E200 (N. Zhang et al., 2013a), and Zi-M650 (Ziethe et al., 2009). The lithosphere at 4.4 Gyr in our reference case is (see the black line in Figure 3a), however, thinner than that in these models (see e.g., Figure 3c in N. Zhang et al. (2013a)). Even in the models where thermally driven mantle convection does not occur at all (Case Ra2.15e4), the lithosphere (see the red line in Figure 3a) is substantially thinner than that in the earlier models KS-S (Konrad & Spohn, 1997; Spohn et al., 2001) and Ln (Laneuville et al., 2013). These differences arise because, in our models, the uppermost mantle is kept hot by melt-fingers and partially molten plumes owing to the matrix-expansion around the fingertip and the melt-buoyancy, respectively. Note that the lithosphere of Case Ra2.15e4 is also thinner than that in a spherically symmetric 1-D model of magma migration in the non-convecting mantle (U et al., 2022) because of heat transport by melt-fingers. Heat transport by melt-fingers and partially molten plumes is an essential part of our models.

Because of the explicit implementation of a model of magma generation and migration into that of mantle convection, our models allow us to infer volcanic history directly from the calculated history of mantle melting. Earlier models have discussed vol-

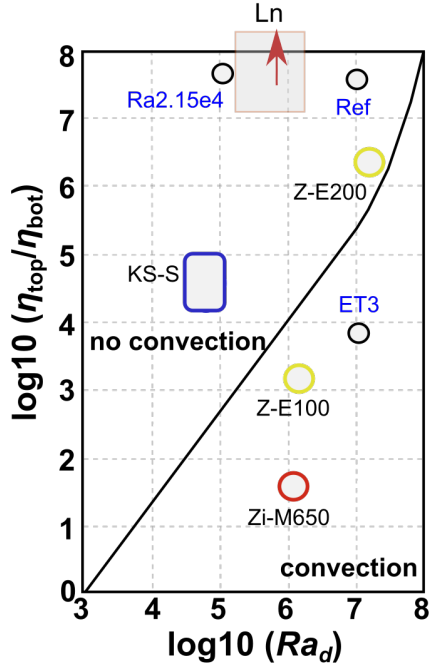


Figure 10. Plots of the critical Rayleigh number for onset of thermal convection in the 3-D spherical mantle heated from the CMB, taken from Figure 8b in Yanagisawa et al. (2016). This viscosity is assumed to depend on the temperature and the magnitude dependence is measured by the viscosity contrast between the surface boundary η_{top} and the CMB η_{bot} . Z-E100 and Z-E200 (the yellow circles) correspond to the case H50E100v5e20 and H50E200v5e20 of N. Zhang et al. (2013a); the brown arrow (Ln) by Laneuville et al. (2013); the red circle (Zi-M650) by the case M650 of Ziethe et al. (2009); the blue rounded rectangle (KS-S) by Konrad and Spohn (1997); Spohn et al. (2001). The black circles (Ref, Ra2.15e4, and ET3) also correspond to the Case Ref, Ra2.15e4, and ET3.

canic history based on the calculated distribution of partially molten regions, especially the depth of the top of the regions and the calculated rate of magma generation in the mantle (e.g., Wood, 1972; Solomon & Toksöz, 1973; Wiczorek & Phillips, 2000; Spohn et al., 2001; Laneuville et al., 2018; U et al., 2022). These models assume that the magma ascends from partially molten regions as deep as 200-800 km to the crust. However, it is not clear if magma eruption is well correlated with the depth and magma generation rate. Magma may not be able to make its way to the surface when the stress state in the lithosphere is horizontally compressive and hence when the planet is contracting (Solomon & Head, 1979; Solomon, 1986). In our models, in contrast, magma rises directly to the base of the crust by melt-fingers and partially molten plumes (Figures 2 and 3), allowing us to predict volcanic history more convincingly. Several issues, however, still remain on magma migration in the crust and the uppermost mantle. It is unclear how mare basaltic magma can ascend through the crust that is not denser than the magma (e.g., Head & Wilson, 1992). The detail of formation of dikes in the uppermost mantle is also important for understanding the magma ascent (e.g., Wilson & Head, 2003, 2017; Head & Wilson, 2017). These issues may be important for also constructing a more refined model of thermal history of the Moon as noted by Lourenço et al. (2018): the thermal history can depend on the ratio of extrusive to intrusive volcanism, which can substantially depend on the porosity, thickness, and density of the crust (e.g., Solomon, 1975; Morota et al., 2009; Taguchi et al., 2017; Head & Wilson, 2020). In future studies, a more refined modeling of magma migration through the crust and the uppermost mantle is needed.

In order to understand the evolution of the compositionally stratified mantle predicted from the hypotheses of the magma ocean and mantle overturn, mass transport by migrating magma and magma-driven convective flow of the mantle is indispensable. The lunar mantle is expected to have been compositionally stratified with a layer enriched in the compositionally dense IBC-component at the base of the mantle after putative crystal fractionation in the magma ocean and subsequent mantle overturn (e.g., Snyder et al., 1992; Hess & Parmentier, 1995; Elkins-Tanton et al., 2011). Some mantle convection models suggest that the basal layer eventually rises as upwelling plumes owing to its thermal buoyancy as the layer is heated by HPEs (e.g., Zhong et al., 2000; Stegman et al., 2003; N. Zhang et al., 2017; W. B. Zhang et al., 2022). In these models, however, the excess composition of the basal layer with respect to the overlying olivine-rich mantle is less than that suggested by some recent models of lunar mantle overturn (e.g., Yu et al., 2019; Zhao et al., 2019), greater than 160 kg m^{-3} (see Figure 6 in H. Li et al. (2019)). At this large compositional density contrast, the basal layer is convectively stable and does not ascend as plumes by thermal buoyancy alone, as inferred from earlier laboratory experiments of mantle convection (see Figure 1 in Le Bars and Davaille (2004)). Although the compositional density contrast in our reference case ($l^* = 4.5$) is around 180 kg m^{-3} (Figure 1), a large fraction of the IBC-rich materials in the layer is extracted and transported to the uppermost mantle by melt-fingers and by partially molten plumes driven by melt-buoyancy (Figure 2); mass transport by migrating magma and melt-buoyancy driven convective flow of the mantle are crucial for understanding the structural evolution of the mantle.

Our model also shows that a careful modeling of HPE transport is important to correctly understand the thermal and volcanic history of lunar mantle. The lunar volcanism has continued until 1-2 Gyr ago (e.g., Hiesinger et al., 2000; Whitten & Head, 2015), and some earlier mantle convection models conclude that the volcanism has continued for such a long period because partially molten regions remained in the cooling mantle for billions of years (Konrad & Spohn, 1997; Spohn et al., 2001; Ziethe et al., 2009). In models where the uppermost mantle is locally more enriched in HPEs, the partially molten regions observed in there persist for more than 3 Gyr (Laneuville et al., 2013, 2014, 2018). Volcanism, however, extracts HPEs from the mantle to let the decline of subsequent volcanic activity (Cassen & Reynolds, 1973; Cassen et al., 1979; Ogawa, 2014, 2018a). In particular, Ogawa (2018a) suggests that partially molten regions disappear within 2

Gyr since the beginning of the calculated history, too short to be a model of the lunar mare volcanism, owing to extraction of HPEs by magmatism. In our models, in contrast, magmatism continues for a much longer time despite that HPE transport by magma is considered (Figures 2 and 3) because a compositionally dense IBC-enriched layer is assumed at the base of the mantle in the initial condition. When HPE- and IBC-enriched materials in the basal layer are transported by melt-fingers and partially molten plumes, the magma often solidifies on the way to the surface and sinks again to the deep mantle (Figure 2; see also Movie S1-4). The initial mantle stratification is necessary for magmatism to continue long. Indeed, in Case No-Mass-tr where a compositionally uniform mantle is assumed in the initial condition ($\xi_b = \xi_e$), the mantle becomes completely solid, and magmatism declines much earlier than that in the reference case (Figure 7).

For a more realistic simulation of the evolution of lunar mantle, it is essential to extend the model to a 3-D spherical shell (e.g., Laneuville et al., 2013; N. Zhang et al., 2017). 2-D annular models of mantle convection tend to predict a higher average temperature in the mantle than 3-D spherical models do, especially when the core size is small, as is the case for the Moon (Guerrero et al., 2018). Although it is computationally challenging, modeling magma generation and migration in a 3-D spherical mantle is a promising avenue for future research.

The dichotomy is also a long-standing issue in studies of mantle dynamics in the Moon (e.g., Jolliff et al., 2000; Lawrence et al., 2000; Cho et al., 2012). Our models show a localized compositional and thermal heterogeneity in the uppermost mantle (Figure 2), but not a global-scale dichotomy like the one that results from an upwelling mantle plume observed in the model of N. Zhang et al. (2013a). Some studies suggest that the lunar dichotomy is caused by an exogenous agent, such as the South Pole-Aitken impact (e.g., Arai et al., 2008; Jones et al., 2022; N. Zhang et al., 2022). It is important to assume the initial condition in which the uppermost mantle in the nearside is more enriched in HPEs than that in the farside (Wieczorek & Phillips, 2000; Laneuville et al., 2013, 2014, 2018).

4.1.2 *The radial expansion/contraction*

Our reference case shows that volume change of the mantle by melting is a key for understanding the radius change of the mantle. To cause the observed early expansion of the Moon, classical earlier models suggest that the initial temperature in the deep mantle was less than 1200 K (Solomon & Chaiken, 1976; Solomon, 1986; Kirk & Stevenson, 1989). This upper limit is, however, substantially lower than that expected from earlier models of mantle overturn that start from giant-impact hypotheses in the literature (e.g., Pritchard & Stevenson, 2000; Canup, 2004; Lock et al., 2018). These overturn models suggest that the initial temperature in the deep mantle is approximately 1800-1900 K (e.g., Hess & Parmentier, 1995; Elkins-Tanton et al., 2011; Boukaré et al., 2018; H. Li et al., 2019). When such a high initial temperature is assumed, the early expansion occurs only nearside (Laneuville et al., 2013) or is much smaller than the observed expansion (N. Zhang et al., 2013a). In a model where the blanket effect in the crust is taken into account (Ziethe et al., 2009; N. Zhang et al., 2013b), thermal expansion of more than 1 km does occur but continues for longer than 1 Gyr, too long to account for the radial expansion of the Moon (e.g., Andrews-Hanna et al., 2013); thermal expansion of the planet continues for such a long period even in our reference case, as shown by the blue line in Figure 4. In our model, however, global expansion occurs by a few kilometers within the first 0.7 Gyr of the calculated history because of melting of the mantle. The radial expansion by melting occurs earlier and is larger than the thermal expansion (Figure 4), suggesting that mantle melting dominates the radial expansion/contraction history of the Moon.

The radial expansion/contraction history depends on the spatial dimensionality. In a 1-D spherically symmetric model where volume change by melting of the mantle is considered, the amplitude of radial expansion is around 1.2 km (see Figure 2 in U et al. (2022)). In contrast, the amplitude in our 2-D model is around 3 km (Figure 4), substantially larger than that in the 1-D model. To predict more quantitatively the radial expansion/contraction history of the Moon, it is necessary to develop a model in a 3-D spherical shell (Laneuville et al., 2013; N. Zhang et al., 2013a, 2013b).

4.2 Comparison with the observed features of the Moon

4.2.1 The radial expansion/contraction

The planet globally expands by a few kilometers for the first several hundred million years in our reference case owing to the volume change caused by melting of the mantle (Figure 4). The timing and amplitude of radial expansion are consistent with those of the Moon inferred from its gravity field in the literature (Andrews-Hanna et al., 2013, 2014; Sawada et al., 2016; Liang & Andrews-Hanna, 2022). After the radial expansion, the planet begins to radially contract at around 1 Gyr after the start of the calculation (Figure 4). The timing of contraction is consistent with the beginning of compressive tectonics on the Moon (Yue et al., 2017; Frueh et al., 2023). The planet in our model contracts at a rate of approximately -1.0 km Gyr^{-1} in the past billion years (Table 3), which is also consistent with the estimates obtained from observations of fault scarps on the Moon (e.g., Watters et al., 2010; Klimczak, 2015; Clark et al., 2017; van der Bogert et al., 2018). As a whole, the calculated history of radius change of the reference case is consistent with that of the Moon. Among our models presented in Figure 8, the radius changes calculated at $M^* \geq 50$, $T_{\text{mid}} \approx 1550 \text{ K}$, and $F_{\text{crst}}^* \leq 16$ are consistent with the observed one. When the reference permeability M^* is lower than 50, the amplitude of radial expansion is much larger than the estimate for the Moon because generated magma in the deep mantle stays there for a long time and is not extracted by melt-fingers (Figures 6 and 8a); melt-fingers are most likely to play an important role in regulating the history of radius change in the Moon. In the cases where the initial concentration ratio of the HPEs in the crust to the mantle F_{crst}^* is larger than 16 (the average heating rate in the mantle is less than 7.6 pW kg^{-1} in the initial condition), sufficient partially molten regions cannot develop to cause the early expansion (Figures 8b). Besides, in order for the early expansion to occur, a substantial fraction of the mantle should be solidified in the initial state (Figures 1a and 8c). Our models also show that the timing and amplitude of radial expansion strongly depend on the presence of overturned IBC-component enriched layer l^* (Figure 8d and Table 3). In Case 10 where the overturned layer is not assumed ($1/l^* = 0$), indeed, the timing and amplitude of calculated radial expansion are later and smaller than the observed expansion.

4.2.2 The volcanic activity

Our reference case is also consistent with the observed history of mare volcanism of the Moon. For the first 0.4 Gyr of the calculated history, the partially molten regions in the deep mantle grow only slowly, while the partially molten region in the uppermost mantle shrinks over time (Figure 2). This early stage is likely to correspond to the period during which mare volcanism on the Moon was not so active (e.g., Hiesinger et al., 2003; Whitten & Head, 2015). The growth of melt-fingers and subsequent partially molten plumes observed in Figure 2b account for the lunar mare volcanism that became active after around 4 Gyr ago and peaked at 3.5-3.8 Gyr ago, and then gradually declined over a period of billions of years (e.g., Hiesinger et al., 2000; Morota et al., 2011); the calculated activity of partially molten plumes is indeed peaked at around 3.7 Gyr ago and then gradually declines with time. In contrast, in a model where plumes do not appear (Case Ra2.15e4 calculated at lower Rayleigh number $Ra = 2.15 \times 10^4$), the volcanic activity develops

only during the first several million years by melt-fingers (Figure 6b), suggesting that partially molten plumes play an important role in the volcanic history of the Moon.

Note that magma not enriched in HPEs is generated in the later period of the calculated history (Figure 2 for 1.44 Gyr). This volcanism is caused by a return flow of a floundering materials enriched in IBC components (see the arrow in Figure 2d). This may account for the volcanism of HPE-depleted young basalts (Che et al., 2021; Q.-L. Li et al., 2021; Su et al., 2022).

4.2.3 The temperature profile

The depth-profile of the horizontally averaged temperature calculated at 4.4 Gyr in our reference case shows that the lithosphere develops as a thermal boundary layer of the convective mantle (Figure 3a), while the temperature profile suggested for the present Moon (e.g., Sonett, 1982; Khan et al., 2006, 2014; Karato, 2013) is closer to a thermal diffusion profile. The difference is not large in the shallow mantle (until the depth level of around 200 km), but the calculated temperature in the mid-mantle is considerably higher than that in the present Moon (Figure 3a). As a consequence, the mantle is partially molten in the mid-mantle (from around $r = 1100$ to 1300 km), whereas seismic evidence suggests that the partially molten region occurs only at the base of the mantle (e.g., Latham et al., 1973; Nakamura et al., 1973; Weber et al., 2011; Tan & Harada, 2021). A temperature profile consistent with the observed one was not obtained at other parameter values (Figure 3a). This difficulty may be a consequence of the assumed 2-D polar rectangular geometry of the convecting vessel and calls for further numerical calculations in a 3-D spherical shell where the mid-mantle tends to be more strongly cooled and mantle convection is more sluggish (Guerrero et al., 2018).

5 Conclusions

To understand the volcanic and radial expansion/contraction history of the Moon, we developed a 2-D polar rectangular numerical model of mantle evolution illustrated in Figure 9. The internally heated mantle of the model evolves by the transport of heat, mass, and heat-producing elements (HPEs) by mantle convection and migrating magma that is generated by decompression melting and internal heating.

Our simulations show that magma generation and migration play a crucial role in the volcanic and radial expansion/contraction history of the Moon. Magma is generated in the deep mantle by internal heating and eventually ascends to the surface as melt-fingers and partially molten plumes driven by melt-buoyancy for the first several hundred million years (Figures 2 and 9). This stage is likely to correspond to the period during which mare volcanism became active after 4 Gyr ago with the peak at 3.5-3.8 Gyr ago (e.g., Whitten & Head, 2015). Subsequent magma ascents by partially molten plumes decline with time but continue for billions of years after the peak because some materials that host HPEs are enriched in the ilmenite-bearing cumulates (IBC) and remain in the deep mantle by their negative buoyancy (Figure 2). This activity accounts for the lunar mare volcanism that gradually declined after the peak (e.g., Hiesinger et al., 2003). The model which accounts for the observed mare volcanism is also consistent with the radial expansion/contraction history of the Moon, which globally expanded in its earlier history until around 3.8 Gyr ago and then contracted with time (e.g., Andrews-Hanna et al., 2013; Frueh et al., 2023). In our model, the planet expands by a few kilometers for the first several hundred million years and then contracts over time (Figure 4). The planetary expansion is due to the extension of partially molten regions by melt-fingers that extract magma generated in the deep mantle (Figures 6a and 8); the subsequent contraction is caused by solidification of the regions due to cooling from the surface boundary. The early expansion by mantle melting suggested here implies that a substantial fraction of the mantle should have been solid, and there was a layer enriched in HPEs and IBC components

at the base of the mantle in the Moon at the beginning of its history (Figures 7-8c, d and Table 3). Further refinement of our model is needed to better understand the thermal history of the Moon. A global-scale lunar dichotomy like the one observed for the Moon does not arise in our models (Figure 2). Some studies propose that it results from external factors, such as the impact that formed South Pole-Aitken basin (e.g., N. Zhang et al., 2022). In order to construct a more realistic thermal history model of the Moon, it is necessary to extend our model to a 3-D spherical shell geometry and to introduce a lateral heterogeneity in the initial thermal and compositional condition in future work.

Appendix A The basic equations

In this section, we describe the basic equations that are not described in the section “Model description”. The continuity equation is

$$\nabla \cdot \mathbf{U} = -\nabla \cdot [\phi(\mathbf{u} - \mathbf{U})] . \quad (\text{A1})$$

The momentum equation for mantle convection is

$$-\nabla P + \rho g + \nabla \cdot [\eta(\nabla \mathbf{U} + {}^t \nabla \mathbf{U})] = 0 . \quad (\text{A2})$$

where the superscript t means transpose of a matrix. Migration of magma is calculated in the energy equation (Katz, 2008),

$$\begin{aligned} \frac{\partial(\rho_0 h)}{\partial t} + \nabla \cdot (\rho_0 h \mathbf{U}) = & -\nabla \cdot [\rho_0 h_1 \phi(\mathbf{u} - \mathbf{U})] - \frac{\Delta v_1}{v_0} \rho_0 g \phi u_r + \nabla \cdot (k \nabla T) \\ & + \rho_0 q + \nabla \cdot [\kappa_{\text{edd}} \nabla(\rho_0 h)] , \end{aligned} \quad (\text{A3})$$

where $h_1 = h(\phi = 1)$. $k = \rho_0 C_p \kappa$ is the thermal conductivity, and κ is the thermal diffusivity. We assumed that the matrix disintegrates and that a strong turbulent diffusion occurs with the eddy diffusivity of $\kappa_{\text{edd}} = 100\kappa$ in largely molten region with $\phi > 0.4$ (Kameyama et al., 1996; Ogawa, 2020). κ_{edd} is assumed to gradually increase with increasing ϕ as ϕ^3 (Ogawa, 2018b; U et al., 2022). We also assumed that the crustal thermal diffusivity is 0.48 times smaller than the mantle thermal diffusivity, taking into account the blanket effect of the crust and regolith layers (Ziethe et al., 2009).

We calculate the phase diagram of the binary eutectic materials $A_\xi B_{1-\xi}$ as well as the temperature, and melt-content from the chemical potential defined for the materials. In the solid phase, the chemical potential μ^{solid} is

$$\mu^{\text{solid}} = -C_p T / \sigma_A - T(S_0 + C_p \ln T / \sigma_A) + P / \rho_0 \quad (\text{A4})$$

for both of the end-members A and B where S_0 is an arbitrary constant. In the liquid state where the melt behaves ideal solution in this model, the chemical potential μ^{liquid} of the end-members i ($i = A, B$) is

$$\mu_i^{\text{liquid}} = \mu_i^{l0} + RT \ln \xi_i^{\text{liquid}} , \quad (\text{A5})$$

and

$$\mu_i^{l0} = \mu^{\text{solid}} + \Delta h / \sigma_i (1 + G - T / T_i^{l0}) . \quad (\text{A6})$$

Here, R is the gas constant $8.3 \text{ J mol}^{-1} \text{ K}^{-1}$; σ_i the molar mass of each end-members ($A = 140.69 \text{ g mol}^{-1}$; $B = 151.71 \text{ g mol}^{-1}$); T_i^{l0} the dry solidus of the end member i at zero-pressure.

The core is regarded as a heat bath of a uniform temperature T_c that changes with time as

$$c_{pc} \rho_{\text{core}} V_{\text{core}} \frac{dT_c}{dt} = -Sf , \quad (\text{A7})$$

where $c_{pc} = 675 \text{ J K}^{-1} \text{ kg}^{-1}$ (Ziethe et al., 2009) is the specific heat of the core, $\rho_{\text{core}} = 6200 \text{ kg m}^{-3}$ (Kronrod et al., 2022) the core density, V_{core} the volume of the core, and S the surface area of the CMB. The heat flux at the CMB f is calculated from

$$f = -\frac{1}{\pi} \int_0^\pi \left(k \frac{\partial T}{\partial r} \right)_{r=r_c} d\theta. \quad (\text{A8})$$

In this study, we neglect the internal heating in the core.

The internal heating rate q changes with time as

$$q = q_{\text{tr}}^* q_0 \exp\left(-\frac{t}{\tau}\right), \quad (\text{A9})$$

where $q_0 = 14.70 \text{ pW kg}^{-1}$ is the average initial heating rate at 4.4 Gyr ago estimated from the total amount of HPEs in the current Moon (see Table 2 in U et al. (2022)); τ the decay time of HPEs. We approximate this value as $\tau = 1.5 \text{ Gyr}$, an average of the decay times of ^{235}U and ^{40}K (Kameyama et al., 1996; Ogawa, 2020). The non-dimensional value q_{tr}^* changes with migrating magma as

$$\frac{\partial q_{\text{tr}}^*}{\partial t} + \nabla \cdot (q_{\text{tr}}^* \mathbf{U}) = -\nabla \cdot [q_1^* \phi (\mathbf{u} - \mathbf{U})] + \nabla \cdot (\kappa_{\text{edd}} \nabla q_{\text{tr}}^*). \quad (\text{A10})$$

Here, q_1^* is the internal heating rate in the melt as

$$q_1^* = \frac{D q_{\text{tr}}^*}{(D-1)\phi + 1}, \quad (\text{A11})$$

and, $D = 100$ is the partition coefficient of HPEs between solid-phase and melt-phase.

The bulk composition ξ_b also changes with time owing to the mass transport by melt and matrix as

$$\frac{\partial \xi_b}{\partial t} + \nabla \cdot (\xi_b \mathbf{U}) = -\nabla \cdot [\xi_1 \phi (\mathbf{u} - \mathbf{U})] + \nabla \cdot [\kappa_{\text{edd}} \nabla (\xi_b)]. \quad (\text{A12})$$

The basic equations are converted into their non-dimensional forms using the length scale $L = r_p - r_c$, the temperature scale $\Delta h / C_p$, and times scale L^2 / κ . The momentum equation in its non-dimensional form is

$$\nabla P^* + Ra \rho^* \mathbf{e}_r + \nabla \cdot [\eta^* (\nabla \mathbf{U}^* + {}^t \nabla \mathbf{U}^*)] = 0. \quad (\text{A13})$$

where

$$\eta^* = \exp [E_T^* (T_{ref}^* - T^*)]. \quad (\text{A14})$$

The non-dimensional relative velocity $\mathbf{u}^* - \mathbf{U}^*$ is written as

$$\mathbf{u}^* - \mathbf{U}^* = -M^* g^* \frac{\phi^2}{\phi_0^3} \frac{\Delta v_l}{v_0} \mathbf{e}_r. \quad (\text{A15})$$

The non-dimensional energy equation is written as

$$\begin{aligned} \frac{\partial h^*}{\partial t} + \nabla \cdot (h^* \mathbf{U}) = & -\nabla \cdot [h_1^* \phi (\mathbf{u}^* - \mathbf{U}^*)] - N^* g^* \frac{\Delta v_l}{v_0} \phi u_r^* + \nabla^2 T^* \\ & + q^* + \nabla \cdot [\kappa_{\text{edd}}^* \nabla (h^*)], \end{aligned} \quad (\text{A16})$$

where $h^* = T^* + \phi(1 + G)$, and $N^* \equiv g_{\text{sur}} L / \Delta h$.

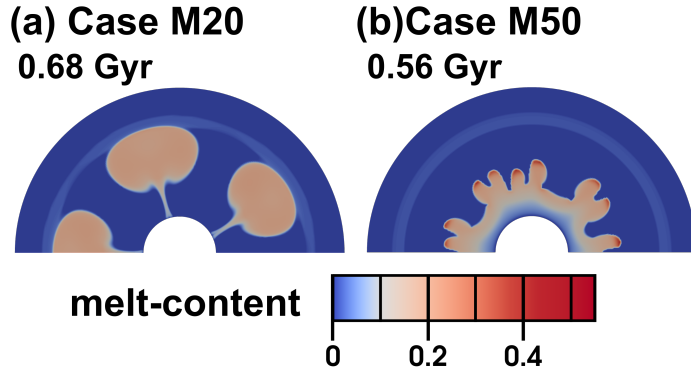


Fig. S1. Snapshots of the distributions of melt-content ϕ calculated in Case (a) M20 and (b) M50. In (b), melt-fingers develop along the top of the partially molten region at a depth.

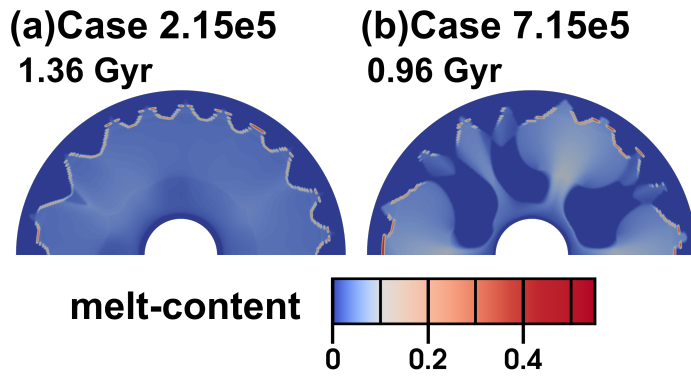


Fig. S2. Snapshots of the distributions of melt-content ϕ calculated in Case (a) Ra2.15e5 and (b) Ra7.15e5. In (b), partially molten plumes develop after the fingertip of melt-fingers reaches the uppermost mantle.

Supporting materials

This supporting information contains snapshots of the distributions of melt-content ϕ calculated in Case M20 and M50 (Figure S1), Ra2.15e5 and Ra7.15e5 (Figure S2), and animations of Case Ref presented in Figures 2-5 of the main article (Movie S1-4). See Table 3 in the main article for case numbers.

The official version of the animations and dataset will be made available after its acceptance by the JGR: Planets. However, the unofficial version of the animations can be accessed through the following links.

Movie S1. An animation of the distributions of temperature T calculated in the reference model (Case Ref). <https://youtu.be/uTTyNOIANb4>

Movie S2. An animation of the distributions of melt-content ϕ calculated in the reference model (Case Ref). <https://youtu.be/FHcj8tZsF3Y>

Movie S3. An animation of the distributions of internal heating rate q calculated in the reference model (Case Ref). <https://youtu.be/nfj9YgnUY8U>

Movie S4. An animation of the distributions of composition ξ_b calculated in the reference model (Case Ref). The blue color stands for the IBC component, while the red color for the olivine-rich end-member. https://youtu.be/jRjIQ9Y_se4

References

- Alley, K. M., & Parmentier, E. M. (1998). Numerical experiments on thermal convection in a chemically stratified viscous fluid heated from below: implications for a model of lunar evolution. *Phys. Earth Planet. Inter.*, *108*(1), 15–32. doi: 10.1016/S0031-9201(98)00096-X
- Andrews-Hanna, J. C., Asmar, S. W., Head III, J. W., Kiefer, W. S., Konopliv, A. S., Lemoine, F. G., ... Zuber, M. T. (2013). Ancient igneous intrusions and early expansion of the moon revealed by grail gravity gradiometry. *Science*, *339*, 675–678. doi: 10.1126/science.1231753
- Andrews-Hanna, J. C., Besserer, J., Head III, J. W., Howett, C. J. A., Kiefer, W. S., Lucey, P. J., ... Zuber, M. T. (2014). Structure and evolution of the lunar procellarum region as revealed by grail gravity data. *Nature*, *514*, 68–71. doi: 10.1038/nature13697
- Arai, T., Terada, H., Yamaguchi, A., & Ohtake, M. (2008). A new model of lunar crust: asymmetry in crustal composition and evolution. *Earth Planets Space*, *60*, 433–444. doi: 10.1186/BF03352808
- Boukaré, C.-E., Parmentier, E. M., & Parman, S. W. (2018). Timing of mantle overturn during magma ocean solidification. *Earth Planet. Sci. Lett.*, *491*(1), 216–225. doi: 10.1016/j.epsl.2018.03.037
- Breuer, D., & Moore, W. (2015). 10.08 - dynamics and thermal history of the terrestrial planets, the moon, and io. *Treatise on Geophysics (Second Edition)*, In G. Schubert (Ed.), 255–305. doi: doi.org/10.1016/B978-0-444-53802-4.00173-1
- Canup, R. M. (2004). Simulations of a late lunar-forming impact. *Icarus*, *168*(2), 433–456. doi: 10.1016/j.icarus.2003.09.028
- Cassen, R., & Reynolds, R. T. (1973). Role of convection in the moon. *J. Geophys. Res.*, *78*(17), 3203–3215. doi: 10.1029/JB078i017p03203
- Cassen, R., Reynolds, R. T., Graziani, F., Summers, A., McNellis, J., & Blalock, L. (1979). Convection and lunar thermal history. *Phys. Earth Planet. Inter.*, *19*(2), 183–196. doi: 10.1016/0031-9201(79)90082-7
- Che, X., Nemchin, A., Liu, T., D. Long, Norman, M. D., Joy, K. H., Tartese, R., ... more (2021). Age and composition of young basalts on the moon, measured from samples returned by chang’e-5. *Science*, *374*(6569), 887–890. doi: 10.1126/science.abl7957

- Cho, Y., Morota, T., Haruyama, J., Yasui, M., Hirata, N., & Sugita, S. (2012). Young mare volcanism in the orientale region contemporary with the procellarum creep terrane (pkt) volcanism peak period around 2 billion years ago. *Geophys. Res. Lett.*, *39*(11). doi: 10.1029/2012GL051838
- Clark, J. M., Jaclyn D. Hurtado Jr., Hiesinger, H., van der Bogert, C. H., & Bernhardt, H. (2017). Investigation of newly discovered lobate scarps: Implications for the tectonic and thermal evolution of the moon. *Icarus*, *298*, 78–88. doi: 10.1016/j.icarus.2017.08.017
- Cuk, M., & Stewart, S. T. (2012). Making the moon from a fast-spinning earth: A giant impact followed by resonant despinning. *Science*, *338*(1047). doi: 10.1126/science.1225542
- de Vries, J., van den Berg, A., & van Westrenen, W. (2010). Formation and evolution of a lunar core from ilmenite-rich magma ocean cumulates. *Earth Planet. Sci. Lett.*, *292*(1-2), 139–147. doi: 10.1016/j.epsl.2010.01.029
- Dumoulin, C., Doin, M.-P., & Fleitout, L. (1999). Heat transport in stagnant lid convection with temperature- and pressure-dependent newtonian or non-newtonian rheology. *J. Geophys. Res. Solid Earth*, *104*(B6), 12759–12777. doi: 10.1029/1999JB900110
- Elkins-Tanton, L., & Bercovici, D. (2014). Contraction or expansion of the moon’s crust during magma ocean freezing? *Philos. Trans. Royal Soc. A*, *372*(20130240). doi: 10.1098/rsta.2013.0240
- Elkins-Tanton, L., Burgess, S., & Yin, Q.-Z. (2011). The lunar magma ocean: reconciling the solidification process with lunar petrology and geochronology. *Earth Planet. Sci. Lett.*, *304*(3–4), 326–336. doi: 10.1016/j.epsl.2011.02.004
- Frueh, T., Hiesinger, H., Bogert, C. H., Clark, J. D., Watters, T. R., & Schmedemann, N. (2023). Timing and origin of compressional tectonism in mare tranquillitatis. *J. Geophys. Res. Planets*, *128*(e2022JE007533). doi: 10.1029/2022JE0075
- Garcia, R. F., Gagnepain-Beyneix, J., Chevrot, S., & Lognonné, P. (2011). Very preliminary reference moon model. *J. Geophys. Res. Planets*, *188*(1-2), 96–113. doi: 10.1016/j.pepi.2011.06.015
- Garcia, R. F., Gagnepain-Beyneix, J., Chevrot, S., & Lognonné, P. (2012). Erratum to “very preliminary reference moon model”. *Phys. Earth Planet. Inter.*, *202-203*, 89–91. doi: 10.1016/j.pepi.2012.03.009
- Guerrero, J. M., Lowman, J. P., Deschamps, F., & Tackley, P. J. (2018). The influence of curvature on convection in a temperature-dependent viscosity fluid: Implications for the 2-d and 3-d modeling of moons. *J. Geophys. Res. Planets*, *123*, 1863–1880. doi: 10.1029/2017JE005497
- Head, J. W., & Wilson, L. (1992). Lunar mare volcanism: Stratigraphy, eruption conditions, and the evolution of secondary crusts. *Geochim. Cosmochim. Acta*, *56*, 2155–2175. doi: 10.1016/0016-7037(92)90183-J
- Head, J. W., & Wilson, L. (2017). Generation, ascent and eruption of magma on the moon: new insights into source depths, magma supply, intrusions and effusive/explosive eruptions (part 2: predicted emplacement processes and observations). *Icarus*, *283*, 176–223. doi: 10.1016/j.icarus.2016.05.031
- Head, J. W., & Wilson, L. (2020). Magmatic intrusion-related processes in the upper lunar crust: The role of country rock porosity/permeability in magmatic percolation and thermal annealing, and implications for gravity signatures. *Planetary and Space Science*, *180*(104765). doi: 10.1016/j.pss.2019.104765
- Hess, P. C., & Parmentier, E. M. (1995). A model for the thermal and chemical evolution of the moon’s interior: implications for the onset of mare volcanism. *Earth Planet. Sci. Lett.*, *134*(3–4), 501–514. doi: 10.1016/0012-821X(95)00138-3
- Hess, P. C., & Parmentier, E. M. (2001). Thermal evolution of a thicker creep liquid layer. *J. Geophys. Res.*, *106*(E11), 28023–28032. doi: 10.1029/2000JE001416

- Hiesinger, H., Head III, J. W., Wolf, U., Jaumann, R., & Neukum, G. (2003). Ages and stratigraphy of mare basalts in oceanus procellarum, mare nubium, mare cognitum, and mare insularum. *J. Geophys. Res. Planets*, *108*(E7), 5065. doi: 10.1029/2002JE001985
- Hiesinger, H., Jaumann, R., Neukum, G., & Head, J. W. (2000). Ages and stratigraphy of mare basalts in oceanus procellarum, mare nubium, mare cognitum, and mare insularum. *J. Geophys. Res. Planets*, *105*(E12), 29239–29275. doi: 10.1029/2000JE001244
- Hosono, N., Karato, S.-i., Makino, J., & R., S. T. (2019). Terrestrial magma ocean origin of the moon. *Nat. Geosci.*, *12*, 418–423. doi: 10.1038/s41561-019-0354-2
- Jolliff, B. L., Gillis, J. J., Haskin L., R. L., Korotev, & Wieczorek, M. A. (2000). Major lunar crustal terranes: Surface expressions and crustal- mantle origins. *J. Geophys. Res.*, *105*(E2), 4197–4216. doi: 10.1029/1999JE001103
- Jones, M. J., Evans, A. J., Johnson, B. C., Weller, M. B., Andrews-Hanna, J. C., Tikoo, S. M., & T., K. J. (2022). A south pole–aitken impact origin of the lunar compositional asymmetry. *Sci. Adv.*, *8*(14). doi: 10.1126/sciadv.abm8475
- Kameyama, M., Fujimoto, H., & Ogawa, M. (1996). A thermo-chemical regime in the upper mantle in the early earth inferred from a numerical model of magma-migration in a convecting upper mantle. *Phys. Earth Planet. Inter.*, *94*(3–4), 187–215. doi: 10.1016/0031-9201(95)03102-2
- Karato, S. (2013). Geophysical constraints on the water content of the lunar mantle and its implications for the origin of the moon. *Earth Planet. Sci. Lett.*, *384*, 144–153. doi: 10.1016/j.epsl.2013.10.001
- Karato, S., & Wu, P. (1993). Rheology of the upper mantle: A synthesis. *Science*, *260*(5109), 771–778. doi: 10.1126/science.260.5109.771
- Katz, R. F. (2008). Magma dynamics with the enthalpy method: Benchmark solutions and magmatic focusing at mid-ocean ridges. *Geochem. Geophys. Geosyst.*, *49*(12), 2099–2121. doi: 10.1093/petrology/egn058
- Katz, R. F., Spiegelman, M., & Langmuir, C. H. (2003). A new parameterization of hydrous mantle melting. *Geochem. Geophys. Geosyst.*, *4*(9), 1073. doi: 10.1029/2002GC000433
- Khan, A., Connolly, J. A. D., Pommier, A., & Noir, J. (2014). Geophysical evidence for melt in the deep lunar interior and implications for lunar evolution. *J. Geophys. Res. Planets*, *119*(10), 2197–2221. doi: 10.1002/2014JE004661
- Khan, A., Maclennan, J., Taylor, S. R., & Connolly, J. A. D. (2006). Are the earth and the moon compositionally alike? inferences on lunar composition and implications for lunar origin and evolution from geophysical modeling. *J. Geophys. Res.*, *111*(E5). doi: 10.1029/2005JE002608
- Kirk, R. L., & Stevenson, D. J. (1989). The competition between thermal contraction and differentiation in the stress history of the moon. *J. Geophys. Res.*, *94*(B9), 12133–12144. doi: 10.1029/JB094iB09p12133
- Klimczak, C. (2015). Limits on the brittle strength of planetary lithospheres undergoing global contraction. *J. Geophys. Res. Planets*, *120*, 2135–2151. doi: 10.1002/2015JE004851
- Konrad, W., & Spohn, T. (1997). Thermal history of the moon: Implications for an early core dynamo and post-accretionary magmatism. *Adv. Space Res.*, *19*(10), 1511–1521. doi: 10.1016/S0273-1177(97)00364-5
- Kronrod, E., Matsumoto, K., Kuskov, O. L., Kronrod, V., Yamada, R., & Kamata, S. (2022). Towards geochemical alternatives to geophysical models of the internal structure of the lunar mantle and core. *Adv. Space Res.*, *69*(7), 2798–2824. doi: 10.1016/j.asr.2022.01.012
- Laneuville, M., Taylor, J., & Wieczorek, M. A. (2018). Distribution of radioactive heat sources and thermal history of the moon. *J. Geophys. Res. Planets*, *123*(12), 3144–3166. doi: 10.1029/2018JE005742

- Laneuville, M., Wieczorek, M. A., Breuer, D., Aubert, J., & Ruckriemen, T. (2014). A long-lived lunar dynamo powered by core crystallization. *Earth Planet. Sci. Lett.*, *401*, 251–260. doi: 10.1016/j.epsl.2014.05.057
- Laneuville, M., Wieczorek, M. A., Breuer, D., & Tosi, N. (2013). Asymmetric thermal evolution of the moon. *J. Geophys. Res. Planets*, *118*(7), 1435–1452. doi: 10.1002/jgre.20103
- Latham, G., Dorman, J., Duennebier, F., Ewing, M., Lammlein, D., & Nakamura, Y. (1973). Moonquakes, meteoroids, and the state of the lunar interior. *Proc. Lunar Sci. Conf.*, *4*, 2515–2527.
- Lawrence, D. J., Feldman, W. C., Barraclough, B. L., Binder, A. B., Elphic, R. C., Maurice, S., . . . Prettyman, T. H. (2000). Small-area thorium features on the lunar surface. *J. Geophys. Res.*, *105*(E8), 20307–20331. doi: 10.1029/1999JE001177
- Le Bars, M., & Davaille, A. (2004). Whole layer convection in a heterogeneous planetary mantle. *J. Geophys. Res. Planets*, *109*(B03403). doi: 10.1029/2003JB002617
- Li, H., Zhang, N., Ling, Y., Wu, B., Dygert, N. K., Huang, J., & Parmentier, E. M. (2019). Lunar cumulate mantle overturn: a model constrained by ilmenite rheology. *J. Geophys. Res. Planets*, *124*(5), 1357–1378. doi: 10.1029/2018JE005905
- Li, Q.-L., Zhou, Q., Liu, Y., Xiao, Z., Lin, Y., Li, J.-H., . . . Li, X.-H. (2021). Two-billion-year-old volcanism on the moon from chang’e-5 basalts. *Nature*, *600*, 54–58. doi: 10.1038/s41586-021-04100-2
- Liang, W., & Andrews-Hanna, J. C. (2022). Probing the source of ancient linear gravity anomalies on the moon. *Icarus*, *380*(114978). doi: 10.1016/j.icarus.2022.114978
- Lock, S., Stewart, S., Petaev, M., Leinhardt, z., Mace, M., Jacobsen, S., & Cuk, M. (2018). The origin of the moon within a terrestrial synestia. *J. Geophys. Res. Planets*, *123*(4), 910–951. doi: 10.1002/2017JE005333
- Lourenço, D. L., Rozel, A. B., Gerya, T., & Tackley, P. J. (2018). Efficient cooling of rocky planets by intrusive magmatism. *J. Geophys. Res.*, *11*, 322–327. doi: 10.1038/s41561-018-0094-8
- Matsuyama, L., Keane, J. T., Trinh, A., Beuthe, M., & Watters, T. R. (2021). Global tectonic patterns of the moon. *Geophys. Res. Lett.*, *358*(114202). doi: 10.1016/j.icarus.2020.114202
- McKenzie, D. (1984). The generation and compaction of partially molten rock. *J. Petrol.*, *25*(3), 713–765. doi: 10.1093/petrology/25.3.713
- Miller, K. J., Zhu, W.-l., Montési, L. G. J., & Gaetani, G. A. (2014). Experimental quantification of permeability of partially molten mantle rock. *Earth Planet. Sci. Lett.*, *388*(15), 273–282. doi: 10.1016/j.epsl.2013.12.003
- Mitchell, R. N. (2021). Chang’e-5 reveals the moon’s secrets to a longer life. *The Innovation*, *2*(4), 100177. doi: doi.org/10.1016/j.xinn.2021.100177
- Morbidelli, A., Nesvornyy, D., Laurenz, V., Marchi, S., Rubie, D. C., Elkins-Tanton, L., . . . Jacobson, S. (2018). The timeline of the lunar bombardment: Revisited. *Icarus*, *305*, 262–276. doi: 10.1016/j.icarus.2017.12.046
- Moriarty III, D. P., Dygert, N., Valencia, S. N., Watkins, R. N., & Petro, N. E. (2021). The search for lunar mantle rocks exposed on the surface of the moon. *Nat. Commun.*, *12*(4659). doi: 10.1038/s41467-021-24626-3
- Morota, T., Haruyama, J., Honda, C., Ohtake, M., Yokota, Y., Kimura, J., . . . Sasaki, S. (2009). Mare volcanism in the lunar farside moscoviense region: Implication for lateral variation in magma production of the moon. *Geophys. Res. Lett.*, *36*(L21202). doi: 10.1029/2009GL040472
- Morota, T., Haruyama, J., Ohtake, M., Matsunaga, T., Kawamura, T., Yokota, Y., . . . Group, L. W. (2011). Timing and duration of mare volcanism in the central region of the northern farside of the moon. *Earth Planets Space*, *63*, 5–11.

- doi: 10.5047/eps.2010.02.009
- Nakamura, Y., Lammlein, D., Latham, G., Ewing, M., Dorman, J., Press, F., & Toksöz, N. (1973). New seismic data on the state of the deep lunar interior. *Science*, *181*(4094), 49–51. doi: 10.1126/science.181.4094.49
- Newsom, H. E., & Taylor, S. R. (1989). Geochemical implications of the formation of the moon by a single giant impact. *Nature*, *338*, 29–34. doi: 10.1038/338029a0
- Ogawa, M. (2014). A positive feedback between magmatism and mantle upwelling in terrestrial planets: Implications for the moon. *J. Geophys. Res. Planets*, *119*, 2317–2330. doi: 10.1002/2014JE004717
- Ogawa, M. (2018a). The effects of magmatic redistribution of heat producing elements on the lunar mantle evolution inferred from numerical models that start from various initial states. *Planet. Space Sci.*, *151*, 43–55. doi: 10.1016/j.pss.2017.10.015
- Ogawa, M. (2018b). Magmatic differentiation and convective stirring of the mantle in early planets: the effects of the magmatism-mantle upwelling feedback. *Geophys. J. Int.*, *215*(3), 2144–2155. doi: 10.1093/gji/ggy413
- Ogawa, M. (2020). Magmatic differentiation and convective stirring of the mantle in early planets – 2: effects of the properties of mantle materials. *Geophys. J. Int.*, *220*(2), 1409–1420. doi: 10.1093/gji/ggz499
- Pritchard, M. E., & Stevenson, D. J. (2000). Thermal aspects of a lunar origin by giant impact. in: Canup rm, righter k (eds) origin of the earth and moon. *Univ. of Ariz. Press, Tucson*, 179–196. doi: 10.2307/j.ctv1v7zdrp
- Rapp, J. F., & Draper, D. S. (2018). Fractional crystallization of the lunar magma ocean: Updating the dominant paradigm. *Meteorit. Planet. Sci.*, *53*(7), 1432–1455. doi: 10.1111/maps.13086
- Ringwood, A. E., & Kesson, S. E. (1976). A dynamic model for mare basalt petrogenesis. *Proc. Lunar Sci. Conf.*, *7*, 1697–1722.
- Rufu, R., Aharonson, O., & Perets, H. B. (2017). A multiple-impact origin for the moon. *Nat. Geosci.*, *10*, 89–94. doi: 10.1038/NGEO2866
- Sawada, N., Morota, T., Kato, S., Ishihara, Y., & Hiramatsu, Y. (2016). Constraints on timing and magnitude of early global expansion of the moon from topographic features in linear gravity anomaly areas. *Geophys. Res. Lett.*, *43*(10), 4865–4870. doi: 10.1002/2016GL068966
- Schwinger, S., & Breuer, D. (2022). Employing magma ocean crystallization models to constrain structure and composition of the lunar interior. *Phys. Earth Planet. Inter.*, *322*. doi: 10.1016/j.pepi.2021.106831
- Shearer, C. K., Hess, P. C., Wieczorek, M. A., Pritchard, M. E., Parmentier, E. M., Borg, L. E., ... Wiechert, U. (2006). Thermal and magmatic evolution of the moon. *Rev Mineral Geochem*, *60*(1), 365–518. doi: doi.org/10.2138/rmg.2006.60.4
- Shearer, C. K., & Papike, J. (1999). Magmatic evolution of the moon. *Am Min*, *84*(1), 1469–1494. doi: 10.2138/am-1999-1001
- Siegler, M. A., & Smrekar, S. E. (2014). Lunar heat flow: Regional prospective of the apollo landing sites. *J. Geophys. Res. Planets*, *119*(1), 47–63. doi: 10.1002/2013JE004453
- Siegler, M. A., Warren, P., Franco, K. L., Paige, D., Feng, J., & White, M. (2022). Lunar heat flow: Global predictions and reduced heat flux. *J. Geophys. Res. Planets*, *127*(e2022JE007182). doi: 10.1029/2022JE007182
- Snyder, G. A., Taylor, L. A., & Neal, C. R. (1992). A chemical model for generating the sources of mare basalts: Combined equilibrium and fractional crystallization of the lunar magmasphere. *Geochim. Cosmochim. Acta*, *56*(10), 3809–3823. doi: 10.1016/0016-7037(92)90172-F
- Solomon, S. C. (1975). Mare volcanism and lunar crustal structure. *Proc. Lunar Sci. Conf.*, *6*, 1021–1042.

- Solomon, S. C. (1986). On the early thermal state of the moon. *Houston, TX, Lunar and Planetary Institute*, 435–452.
- Solomon, S. C., & Chaiken, J. (1976). Thermal expansion and thermal stress in the moon and terrestrial planets: clues to early thermal history. *Proc. Lunar Sci. Conf.*, 7, 3229–3243.
- Solomon, S. C., & Head, J. W. (1979). Vertical movement in mare basins: Relation to mare emplacement, basin tectonics, and lunar thermal history. *J. Geophys. Res.*, 84(B4), 1667–1682. doi: 10.1029/JB084iB04p01667
- Solomon, S. C., & Toksöz, M. N. (1973). Internal constitution and evolution of the moon. *Phys. Earth Planet. Inter.*, 7(1), 15–38. doi: 10.1016/0031-9201(73)90037-X
- Sonett, C. P. (1982). Electromagnetic induction in the moon. *Rev. Geophys.*, 20(3). doi: 10.1029/RG020i003p00411
- Spohn, T., Konrad, W., Breuer, D., & Ziethe, R. (2001). The longevity of lunar volcanism: implications of thermal evolution calculations with 2d and 3d mantle convection models. *Icarus*, 149(1), 54–65. doi: 10.1006/icar.2000.6514
- Stegman, D. R., Jellinek, A. M., Zatman, S. A., Baumgardner, J. R., & Richards, M. A. (2003). An early lunar core dynamo driven by thermochemical mantle convection. *Nature*, 421, 143–146.
- Stevenson, D. J. (1987). Origin of the moon—the collision hypothesis. *Annu. Rev. Earth Planet. Sci.*, 15, 271–315. doi: 10.1146/annurev.ea.15.050187.001415
- Su, B., Y. J., Chen, Y., Yang, W., Mitchell, R. N., Hui, H., Wang, H., . . . Wu, F.-Y. (2022). Fusible mantle cumulates trigger young mare volcanism on the cooling moon. *Sci. Adv.*, 8(42). doi: 10.1126/sciadv.abn2103
- Taguchi, M., Morota, T., & Kato, S. (2017). Lateral heterogeneity of lunar volcanic activity according to volumes of mare basalts in the farside basins. *J. Geophys. Res. Planets*, 122(7), 1505–1521. doi: 10.1002/2016JE005246
- Tan, Y., & Harada, Y. (2021). Tidal constraints on the low-viscosity zone of the moon. *Icarus*, 365(114361). doi: 10.1016/j.icarus.2021.114361
- Toksöz, M. N., & Solomon, S. C. (1973). Thermal history and evolution of the moon. *The Moon*, 7, 251–278.
- U, K., Hasumi, H., & Ogawa, M. (2022). Effects of magma-generation and migration on the expansion and contraction history of the moon. *Earth Planets Space*, 74(78). doi: 10.1186/s40623-022-01631-4
- van der Bogert, C. H., Clark, J. D., Hiesinger, H., Banks, M. E., Watters, T. R., & Robinson, M. S. (2018). How old are lunar lobate scarps? 1. seismic resetting of crater size-frequency distributions. *Icarus*, 306, 225–242. doi: 10.1016/j.icarus.2018.01.019
- Vander Kaaden, K. E., Agee, C. B., & McCubbin, F. M. (2015). Density and compressibility of the molten lunar picritic glasses: Implications for the roles of ti and fe in the structures of silicate melts. *Geochim. Cosmochim. Acta*, 149, 1–20. doi: 10.1016/j.gca.2014.10.029
- Viswanathan, V., Rambaux, N., Fienga, A., Laskar, J., & M., G. (2019). Observational constraint on the radius and oblateness of the lunar core-mantle boundary. *Geophys. Res. Lett.*, 46(13), 7295–7303. doi: 10.1029/2019GL082677
- Watters, T. R., Robinson, M. S., Beyer, R. A., Banks, M. E., Bell, J. F., Pritchard, M. E., . . . Williams, N. R. (2010). Evidence of recent thrust faulting on the moon revealed by the lunar reconnaissance orbiter camera. *Science*, 329(5994), 936–940. doi: 10.1126/science.1189590
- Watters, T. R., Robinson, M. S., Collins, G. C., Banks, M. E., Daud, K., Williams, N. R., & Selvens, M. M. (2015). Global thrust faulting on the moon and the influence of tidal stresses. *Geology*, 43(10), 851–854. doi: 10.1130/G37120.1
- Weber, R. C., Lin, P.-Y., Garnero, E. J., Williams, Q., & Lognonné, P. (2011). Seismic detection of the lunar core. *Science*, 331(6015), 309–312. doi: 10.1126/science.1199375

- Whitten, J. L., & Head, J. W. (2015). Lunar cryptomaria: Physical characteristics, distribution, and implications for ancient volcanism. *Icarus*, *247*, 150–171. doi: 10.1016/j.icarus.2014.09.031
- Wieczorek, M. A., Neumann, G. A., Nimmo, F., Kiefer, W. S., Taylor, G. J., Melosh, R. J., H. J. abd Phillips, . . . Zuber, M. T. (2013). The crust of the moon as seen by grail. *Science*, *339*(6029), 671–675. doi: 10.1126/science.1199375
- Wieczorek, M. A., & Phillips, R. J. (2000). The “procellarum creep terrane”: Implications for mare volcanism and lunar evolution. *J. Geophys. Res. Planets*, *105*(E8), 20417–20430. doi: 10.1029/1999JE001092
- Wilson, L., & Head, J. W. (2003). Deep generation of magmatic gas on the moon and implications for pyroclastic eruptions. *Icarus*, *30*(12). doi: 10.1029/2002GL016082
- Wilson, L., & Head, J. W. (2017). Generation, ascent and eruption of magma on the moon: new insights into source depths, magma supply, intrusions and effusive/explosive eruptions (part 1: theory). *Icarus*, *283*, 146–175. doi: 10.1016/j.icarus.2015.12.039
- Wood, J. A. (1972). Thermal history and early magmatism in the moon. *Icarus*, *16*(2), 229–240. doi: 10.1016/0019-1035(72)90070-X
- Yan, J., Xu, L., Li, F., Matsumoto, K., Rodriguez, J. A. P., Miyamoto, H., & Dohm, J. M. (2015). Lunar core structure investigation: Implication of GRAIL gravity field model. *Adv. Space Res.*, *55*(6), 1721–1727. doi: 10.1016/j.asr.2014.12.038
- Yanagisawa, T., Kameyama, M., & Ogawa, M. (2016). Numerical studies on convective stability and flow pattern in three-dimensional spherical mantle of terrestrial planets. *Geophys. J. Int.*, *206*(3), 1526–1538. doi: 10.1093/gji/ggw226
- Yu, S., Tosi, N., Schwinger, S., Maurice, M., Breuer, D., & Xiao, L. (2019). Overturn of ilmenite-bearing cumulates in a rheologically weak lunar mantle. *J. Geophys. Res. Planets*, *124*(2), 418–436.
- Yue, Z., Michael, G. G., Di, K., & Liu, J. (2017). Global survey of lunar wrinkle ridge formation times. *Earth Planet. Sci. Lett.*, *477*, 14–20. doi: 10.1016/j.epsl.2017.07.048
- Zhang, N., Ding, M., Zhu, M.-H., Li, H., Li, H., & Yue, Z. (2022). Lunar compositional asymmetry explained by mantle overturn following the south pole–aitken impact. *Nat. Geosci.*, *15*, 37–41. doi: 10.1038/s41561-021-00872-4
- Zhang, N., Dygert, N., Liang, Y., & Parmentier, E. (2017). The effect of ilmenite viscosity on the dynamics and evolution of an overturned lunar cumulate mantle. *Geophys. Res. Lett.*, *44*, 6543–6552. doi: 10.1002/2017GL073702
- Zhang, N., Parmentier, E., & Liang, Y. (2013a). A 3-d numerical study of the thermal evolution of the moon after cumulate mantle overturn: the importance of rheology and core solidification. *J. Geophys. Res. Planets*, *118*(9), 1789–1804. doi: 10.1002/jgre.20121
- Zhang, N., Parmentier, E., & Liang, Y. (2013b). Effects of lunar cumulate mantle overturn and megaregolith on the expansion and contraction history of the moon. *Geophys. Res. Lett.*, *40*(19), 5019–5023. doi: 10.1002/grl.50988
- Zhang, W. B., Zhang, N., & Li, H. Y. (2022). Abundances of lunar heat-producing elements constrained by a 3-d numerical model of titanium-rich basaltic eruption. *Chinese J. Geophys.*, *65*(1), 119–136. doi: 10.6038/cjg2022P0753
- Zhao, Y., de Vries, J., van den Berg, A. P., Jacobs, M. H. G., & van Westrenen, W. (2019). The participation of ilmenite-bearing cumulates in lunar mantle overturn. *Earth Planet. Sci. Lett.*, *511*(1), 1–11. doi: 10.1016/j.epsl.2019.01.022
- Zhong, S., Parmentier, E. M., & Zuber, M. T. (2000). A dynamic origin for the global asymmetry of lunar mare basalts. *Earth Planet. Sci. Lett.*, *177*(3–4), 131–140. doi: 10.1016/S0012-821X(00)00041-8
- Ziethe, R., Seiferlin, K., & Hiesinger, H. (2009). Duration and extent of lunar vol-

canism: Comparison of 3d convection models to mare basalt ages. *Planet. Space Sci.*, 57(7), 784–796. doi: 10.1016/j.pss.2009.02.002

Acknowledgments

The authors would like to thank T. Yanagisawa and T. Miyagoshi at JAMSTEC for their constructive comments. This work was supported by JST SPRING, Grant Number JPMJSP2108 of Japan. Movie S1-4 and Figures 2, 5-7, and S1-S2 were drawn with the ParaView by Sandia National Laboratory, Kitware Inc., and Los Alamos National Laboratory.